Evaluation of precipitation products for small karst catchment hydrological modeling in data-scarce mountainous regions

Ibrahim Al Khoury, Laurie Boithias, Vianney Sivelle, Ryan Bailey, Salam Abbas, Paolo Filippucci, Christian Massari, David Labat

Journal of Hydrology 645 (2024) 132131

Contents lists available at ScienceDirect

Journal of Hydrology

journal homepage: www.elsevier.com/locate/jhydrol

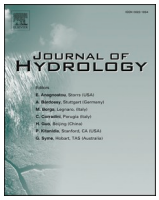

Research papers

Evaluation of precipitation products for small karst catchment hydrological modeling in data-scarce mountainous regions

Ibrahim Al Khoury [a,*], Laurie Boithias [a], Vianney Sivelle [b], Ryan T. Bailey [c], Salam A. Abbas [c], Paolo Filippucci [b], Christian Massari [b], David Labat [a]

[a] Géosciences Environnement Toulouse, Université de Toulouse 3, CNRS, IRD, UPS, France
[b] Research Institute for Geo-Hydrological Protection, National Research Council, Perugia, Italy
[c] Department of Civil and Environmental Engineering, Colorado State University, 1372 Campus Delivery, Fort Collins, CO, USA

ARTICLE INFO

This manuscript was handled by Corrado Corradini, Editor-in-Chief, with the assistance of Xuan Yu, Associate Editor

Keywords:
Karst catchment
Pyrenees Mountain range
Satellite precipitation
Reanalysis precipitation
ISPEEKH

ABSTRACT

The accuracy of gauge-based, satellite-based and reanalysis precipitation products for streamflow simulation has rarely been investigated in data-scarce and meso-scale karst catchments characterized by infra-daily response time due to the predominance of quick flow processes. This study evaluates and compares the reliability of gauge- and satellite-based precipitation products (CPC, E-OBS, PERSIANN-CDR, IMERG-LR, SM2RAIN-ASCAT, CHIRPS) and reanalysis products (SAFRAN, COMEPHORE, ERA5-Land) in simulating the daily flow of the Baget karst catchment (13.25 km^2), located in the Southwestern French Pyrenees. The assessment was conducted over the 2006–2018 period using the semi-distributed karst hydrogeological model ISPEEKH, integrated with a PEST framework for model calibration, global sensitivity analysis using the Morris method, and parameter estimation using an iterative ensemble smoother form of the Gauss-Levenberg-Marquardt algorithm. The discharge coefficients and emptying exponents of the epikarst-to-conduit and conduit-to-spring quick flows were the most sensitive model parameters irrespective of the input precipitation, and ISPEEKH successfully reproduced the non-linear conduit flow dynamics in the catchment. Yet, simulated streamflow was significantly underestimated under the ensemble of precipitation products (up to 32–79 % in the calibration period and up to 28–70 % in the validation period), and the reanalysis products outperformed the gauge- and satellite-based products. Downscaling of the CPC, IMERG-LR, ERA5-Land and E-OBS products, and merging of the CPC and IMERG-LR datasets at 1-km spatial resolution did not improve the model predictive performance. Finally, the study showed that watershed-scale precipitation correction can effectively improve the hydrological simulation performance in the catchment, particularly under the French reanalysis precipitation product COMEPHORE. This result emphasizes the need to install representative rain gauge stations at different altitudes in studied karst catchments of similar scale and hydrodynamics characteristics, and apply observation-based correction methods in order to reduce the errors in regional reanalysis precipitation database and optimize the karst discharge simulation.

1. Introduction

Karst landscapes, formed by chemical dissolution of soluble carbonate rocks by acid water enriched with carbon dioxide, cover nearly 15.2 % of the Earth's ice-free continental surface (Goldscheider et al., 2020) and supply groundwater to 9–25 % of the world's population (Chen et al., 2017; Stevanović, 2019). Compared to granular aquifers, the hydrological behavior of karst aquifers is highly complex, non-linear, and non-stationary (An et al., 2020; Labat et al., 2000a). Karst aquifers exhibit dual-to-triple porosity with discrete conduit networks embedded in a larger fissured matrix. They are characterized by dual recharge and discharge mechanisms, including diffuse infiltration through the matrix and slow-flow discharge into the spring, primarily in the low-flow periods, and concentrated infiltration into secondary porosity features (i.e., fissures, channels, conduits, fractures and sinkholes), with quick-flow discharge into the spring during the wet periods or after a significant recharge event (Geyer et al., 2013; Paiva and Cunha, 2020). A bidirectional matrix-conduit exchange flow can also

* Corresponding author.
E-mail address: ibrahim.al-khoury@get.omp.eu (I. Al Khoury).

https://doi.org/10.1016/j.jhydrol.2024.132131
Received 17 June 2024; Received in revised form 24 September 2024; Accepted 26 September 2024
Available online 10 October 2024

occur due to the head difference between the two domains (Dal Soglio et al., 2020; Zhao et al., 2021). Moreover, karst aquifers often encompass an uppermost weathered zone of carbonate rocks with high porosity and permeability, called epikarst, which stores water and controls the recharge towards the matrix and conduits (Bailly-Comte et al., 2008; Fidelibus et al., 2017). These hydrogeological characteristics render karst aquifers flow very sensitive to changes in precipitation patterns and recharge rates induced by climate change, land-use change, and other anthropogenic activities impacting groundwater storage (Fiorillo and Guadagno, 2012; Klaas et al., 2020; Mo et al., 2023; Nerantzaki and Nikolaidis, 2020; Ruiz et al., 2022; Taheri et al., 2016). Therefore, the adequate management of water resources in karst watersheds requires a sufficient understanding of their recharge and discharge dynamics, coupled with an accurate assessment of their water balance using karst-specific hydrological modeling tools.

Hydrological models aim to approximate the transfer function between meteorological forcing (i.e., precipitation, temperature, potential evapotranspiration) and river streamflow (or spring discharge). One common approach for hydrological modeling consists of considering different combinations of the dominant flow components as distinct conceptual buckets. This approach has been widely developed during the past decades (Azimi et al., 2023; Bittner et al., 2018; Butscher and Huggenberger, 2008; Fleury et al., 2007, 2009; Mazzilli et al., 2019; Sivelle et al., 2023; Tritz et al., 2011) and applied to simulate karst spring discharge and further assess the impact of groundwater abstraction (Cousquer and Jourde, 2022; Labat et al., 2022) and climate change (Hartmann et al., 2012; Sivelle et al., 2021) on karst water resources. However, by neglecting the spatial variabilities of the meteorological forcing and landscape characteristics (i.e., topography, karst terrains, soil and land use), lumped models may lack precision in assessing the intricate recharge and discharge within karst aquifers, hindering accurate flow prediction and data-driven karst water resources management. On the other hand, fully-distributed models discretize karst watersheds into two- or three-dimensional grid units assigned with specific hydraulic parameters and simulate flow between these computational units using differential equations. These models, however, require an adequate knowledge of the geological settings (lithology, fractures, faults) and hydraulic properties (porosity, hydraulic conductivity), which are highly heterogeneous in karst aquifers and can be challenging or impossible to acquire (Fischer et al., 2018; Ghasemizadeh et al., 2012; Gill et al., 2021; Jeannin et al., 2021). Thus, semi-distributed hydrogeological models are proposed as a hybrid approach to overcome the limitations of the aforementioned two model classes by combining the spatial variability of the surface flow dominant controls (i.e., climatic features, landscape properties) with the underlying karst aquifer dominant flow components (Hartmann et al., 2013; Ollivier et al., 2020).

Precipitation is one of the key driving factors in the hydrological modeling of the watershed water balance fluxes. Numerous studies have demonstrated the dependence of the predictive capability of hydrological models for basin streamflow simulation on the input precipitation data (Bárdossy et al., 2022; Camici et al., 2018; Maggioni and Massari, 2018), as well as on the spatial discretization of the precipitation field from lumped to distributed, showing results that vary with the watershed physiographic and climatic properties. By assessing the hydrological response of an ensemble of basins to the precipitation variability (i.e., complete precipitation field and sampled precipitation) and rainfall-runoff modeling approaches (i.e., lumped and distributed), Arnaud et al. (2011) concluded that the small catchments were mostly sensitive to the precipitation input uncertainties produced by sampling of precipitation, while the largest catchments were sensitive to the uncertainties generated by discarding the spatial variability of precipitation. Lobligeois et al. (2014) also evaluated streamflow simulation for an ensemble of catchments using lumped and semi-distributed models driven by 1-km resolution precipitation, and showed that differences in model performance were insignificant between lumped and semi-distributed approaches but highly variable between catchments due to the spatial heterogeneity of the precipitation fields. In addition, Emmanuel et al. (2017) found that higher spatial resolution of precipitation could improve model performance, while Huang et al. (2019) concluded that streamflow simulations improved marginally with higher precipitation spatial resolution and were more sensitive to the temporal resolution of precipitation. These findings underscore the importance of identifying the most suitable precipitation estimate for hydrological applications.

The sparse distribution of rain gauges in watersheds poses challenges for hydroclimatic analysis, prompting the need for alternative precipitation inputs for streamflow simulation. Apart from gauge-based precipitation, recent developments in Earth observation and atmospheric reanalysis have provided long-term precipitation datasets with comparable or even broader spatial coverage than in-situ station observations. In this regard, there are two main categories of satellite precipitation products: those that infer precipitation from clouds and atmosphere characteristics (Top-Down approach), such as PERSIANN-CDR (0.25° spatial resolution; Ashouri et al., 2015) and IMERG (0.1° resolution, Huffman et al., 2019), and those that infer precipitation from the variation of soil moisture (Bottom-Up approach), such as SM2RAIN-ASCAT (0.1° resolution, Brocca et al., 2019). Moreover, reanalysis data such as ERA5 (0.25° resolution; Hersbach et al., 2020) and COMEPHORE (1-km resolution; Tabary et al., 2012) are commonly used. However, these precipitation products can generate biased streamflow forecasts due to various error sources (Aryal et al., 2023; Bitew et al., 2012; Dos Reis et al., 2017; Peinó et al., 2024; Satgé et al., 2019; Zhang et al., 2020), which hinders their application in assessing the hydrological response of karst watersheds characterized by fast aquifer recharge and dominant conduit flow to changing climate conditions.

Currently, there are very few studies that examine the impact of various precipitation inputs from satellite and reanalysis data products on streamflow simulation in karstified watersheds (Chang et al., 2024; Furl et al., 2018; Gan et al., 2020, 2021; Li et al., 2019; Mo et al., 2020, 2022; Wang et al., 2017). Most of these studies were conducted in China, being one of the largest karst areas in the world, across watersheds ranging from 10^3 to 10^5 km^2. Nonetheless, karst watersheds in Europe are often characterized by smaller recharge areas; for instance, the largest karst spring in Europe, Fontaine de Vaucluse, has a recharge area of around 1,160 km^2 (Ollivier et al., 2019). Of the studies reported in the literature, Mo et al. (2020) evaluated the suitability of coarse and corrected IMERG satellite precipitation for daily and monthly streamflow simulation in the XiaJia River basin (799.2 km^2) using the SWAT model. Results showed that SWAT performance under the original IMERG rainfall dataset was unsatisfactory due to major streamflow underestimation, while corrected IMERG precipitation significantly improved the simulations. Mo et al. (2022) simulated streamflow of the Chengbi River basin (2,087 km^2) using SWAT driven by gauge-measured precipitation, IMERG precipitation, and 1-km resolution precipitation derived by geographical weighted regression (GWR) fusion of the measured and IMERG data. The station-measured precipitation data performed best, followed by the GWR fusion precipitation dataset, while the IMERG satellite precipitation yielded the worst performance, highlighting the significance of fusion processing to improve streamflow simulation at the daily and monthly scales. Thus, there is a notable research gap associated with assessing the accuracy of gauge-based, satellite-based or reanalysis precipitation products for the hydrological modeling of meso-scale karst basins (approximately 10–10^3 km^2; Uhlenbrook et al., 2004), using distributed or semi-distributed hydrological models. To the best of our knowledge, this is the first study that aims to evaluate and compare the reliability of reanalysis, gauge-, and satellite-based precipitation products, at coarse (tens of kilometer) and 1-km (downscaled) spatial resolution, for the daily water balance and streamflow simulation in a meso-scale karst catchment with a short response time to precipitation and a sparse precipitation monitoring network. The Baget karst catchment (13.25 km^2) in the piedmont of the Pyrenees mountains, southwest of France, serves as the study area. The semi-distributed karst hydrogeological model ISPEEKH (Al Khoury et al., 2023), a modified version

of SWAT+ (Bieger et al., 2017) for spring flow-dominated karst watersheds, was used to simulate the hydrological response of the Baget catchment to the different precipitation datasets over the years 2006–2018. ISPEEKH was integrated with a Parameter ESTimation Tool (PEST) framework in order to perform automated calibration, identify model parameters that influence the streamflow simulation using the Morris method for global sensitivity analysis, and estimate the model parameter values using an iterative ensemble smoother (iES) form of the Gauss-Levenberg-Marquardt algorithm.

2. Methods and materials

2.1. Study area

The Baget is a karst catchment in the Pyrenees mountains, southwest of France (station B1 at 42°57′18.06″N; 1°1′52.76″E) (Fig. 1). It is part of the KARST National Observatory Service (SNO KARST, Jourde et al., 2018) and part of the French network of Critical Zone Observatories Research and Applications–National Research Infrastructure (OZCAR, Gaillardet et al., 2018). The Baget catchment has a groundwater recharge contribution zone of about 13.25 km^2 and is characterized by a rapid infiltration, a fast transit time between recharge and discharge, and a strong nonlinear rainfall-runoff relationship (Labat et al., 1999, 2000a). The geology within the catchment consists of a mixed lithological terrain: Jurassic and Cretaceous karstified landforms (67 % of the recharge area) and non-karstified rocks (33 % of the recharge area). The large carbonate part of the catchment includes a crystalline limestone band and Jurassic dolomites (Debroas, 2009).

The Baget catchment is exposed to an Atlantic oceanic climate with mountainous influence. The mean daily air temperature is 12 ± 6.3 °C and the mean annual precipitation is 975.5 mm based on the records of the Saint Girons meteorological station (43°00′19″N; 01°06′25″E; 414 m a.s.l). The catchment's snowpack is generally low, and snowmelt does not significantly contribute to discharge (Padilla et al., 1994; Richieri et al., 2024; Ulloa-Cedamanos et al., 2020).

The catchment's streamflow is primarily formed by the perennial karst spring Las Hountas through well-developed conduit networks and partially by the Lachein stream, which drains the impermeable terrains in the catchment. The mean catchment discharge measured at the outlet gauging station B1 was 0.44 ± 0.67 m^3.s^{-1}. Tracer tests (Sivelle and Labat, 2019) and lumped-parameter hydrological modeling of the Baget karst system (Sivelle et al., 2019; Shirafkan et al., 2023) show that nonlinear conduit flow is the main component of the karst spring discharge.

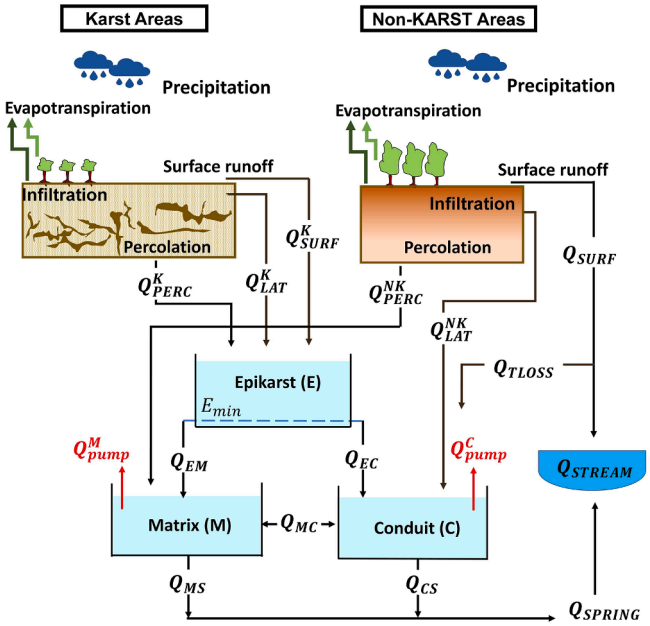

Fig. 2. Schematic representation of the hydrological processes simulated by ISPEEKH in a spring flow-dominated karst watershed (modified from Al Khoury et al., 2023).

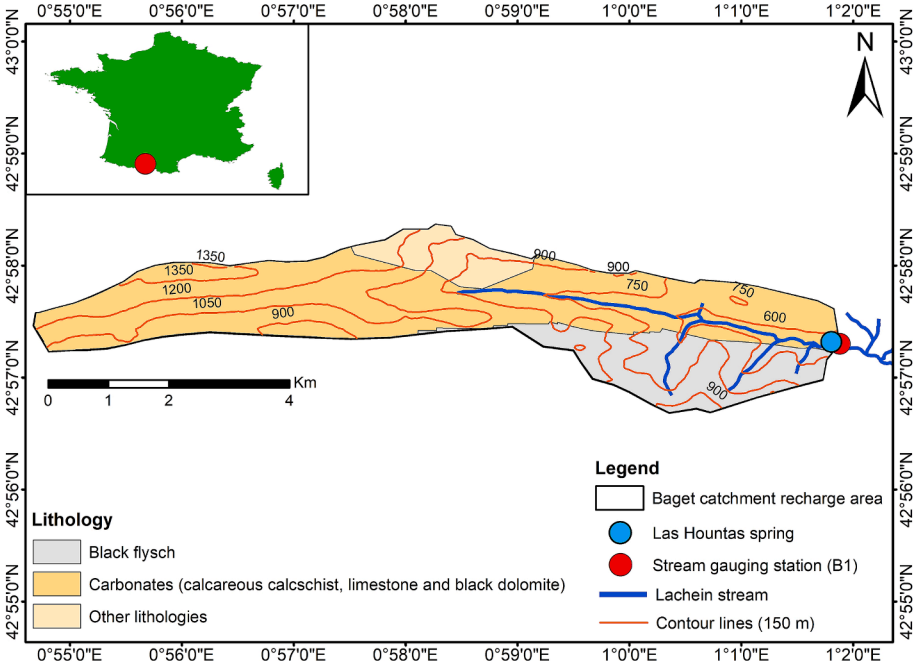

Fig. 1. The Baget catchment recharge area and lithological composition, with the Las Hountas karst spring, the Lachein stream, and the stream gauging station (B1) (modified from Al Khoury et al., 2023).

2.2. The ISPEEKH model

The Integration of Surface ProcEssEs in Karst Hydrology (ISPEEKH) is a semi-distributed karst hydrological model (Fig. 2, Al Khoury et al., 2023) that was developed by modifying the source code of SWAT+ (revision 60.5.4), the restructured version of the Soil and Water Assessment Tool (SWAT) (Bieger et al., 2017). It was used in the study as other modified SWAT-based models reported in the literature and applied in karst hydrology (e.g., Baffaut and Benson, 2009; Geng et al., 2021; Nerantzaki et al., 2020; Nikolaidis et al., 2013; Nguyen et al., 2020; Palanisamy and Workman, 2015; Wang and Brubaker, 2014; Wang et al., 2019;Yactayo, 2009; Zhou et al., 2022) do not collectively reproduce the flow processes of the epikarst, matrix and conduits, including the matrix-conduit bidirectional exchange flow rate, using non-linear storage-discharge relationships (Al Khoury et al., 2023).

ISPEEKH uses input digital elevation model (DEM), land-use map, and overlapped soil and lithology maps to divide the watershed into subbasins connected through stream channels and further into hydrological response units (HRUs) of homogeneous land-use, slope, soil, and karst/non-karst landform properties. It then utilizes spatially-variable weather input data (i.e., precipitation, minimum and maximum air temperature, solar radiation, wind speed, and relative humidity) to simulate the daily vadose zone water balance fluxes at the HRU scale. The land surface and soil hydrological fluxes, including potential evapotranspiration (Monteith, 1965), actual evapotranspiration (sum of canopy evaporation, soil evaporation, and plant transpiration), direct (surface) runoff method (USDA-SCS, 1972), lateral flow (Sloan and Moore, 1984), and percolation (Neitsch et al., 2011) are simulated in ISPEEKH using the original SWAT+ subroutines. SWAT differentiates between solid and liquid precipitation based on near-surface air temperature. If the snowfall temperature parameter is lower than the mean daily air temperature, precipitation is classified as snow. When precipitation is considered solid, it accumulates at the ground surface until snowmelt, which is influenced by air and snowpack temperature, daylight hours, and snow areal coverage. A detailed description of the vadose zone water balance fluxes and corresponding equations applied in standard SWAT+ is provided in the SWAT theoretical manual (Neitsch et al., 2011).

To represent the flow in the saturated zone, the diffusive recharge equations and linear reservoir model for baseflow simulation in granular-type aquifers in SWAT+ were modified in ISPEEKH into diffusive and concentrated recharge equations and a non-linear three-reservoir model of the epikarst, matrix and conduits water bearing components of karst aquifers. Thus, ISPEEKH applies three non-linear reservoirs organized in a two-level structure: the upper reservoir (E) representing the epikarst zone, and the lower reservoirs (M) and (C) that represent the low-permeability matrix and highly permeable conduits, respectively. For karst-dominated catchments characterized by low surface runoff generation and significant spring flow contribution to the overall discharge, ISPEEKH considers direct rainfall infiltration without surface runoff generation over the surface-exposed and well-developed epikarstic zone, with lateral flow down hillslopes and soil water percolation in areas where the soil covers the epikarst (Equation (1)). Water percolation from the soil profile in non-karst HRUs recharges the matrix reservoir diffusively (Equation (2)), while soil lateral flow generated in non-karst areas and water losses from sinking channels seep directly into the conduit reservoir (Equation (3)). The simulated groundwater fluxes include: fast recharge from the epikarst to conduits (Q_{EC}) and slow recharge from the epikarst to the matrix (Q_{EM}), which are activated when the water level of reservoir E exceeds a lower storage threshold (E_{min}), the conduit quick-flow (Q_{CS}) and matrix slow-flow (Q_{MS}) components of the karst spring discharge, and the conduit-matrix bidirectional exchange flow rate (Q_{MC}) as a function of the difference between the water levels of the two reservoirs M and C. The water balance of the reservoirs E, M and C are represented by Equations (4), (5) and (6), respectively. The model can also account for user input daily groundwater abstraction (pumping) data from the matrix and / or conduits. Spring flow from the karst aquifer (Q_{SPRING}) is finally added to surface runoff generated over the non-karst areas (Q_{SURF}) to form the total catchment discharge downstream the karst spring outlet(s) (Equation (7)).

$$RECH_{E,i} = RECH_{E,i-1} \times e^{-\frac{1}{\delta_E}} + \left(1 - e^{-\frac{1}{\delta_E}}\right) \times \sum_{j=1}^{nhrus-K} \left(Q^{K}_{SURF,i,j} + Q^{K}_{LAT,i,j} + Q^{K}_{PERC,i,j}\right) \quad (1)$$

$$RECH_{M,i} = RECH_{M,i-1} \times e^{-\frac{1}{\delta_M}} + \left(1 - e^{-\frac{1}{\delta_M}}\right) \times \sum_{j=1}^{nhrus-NK} Q^{NK}_{PERC,i,j} \quad (2)$$

$$RECH_{C,i} = Q_{TLOSS,i} + \sum_{j=1}^{nhrus-NK} Q^{NK}_{LAT,i,j} \quad (3)$$

where $RECH_{E,i}$ and $RECH_{E,i-1}$ represent the recharge to the epikarst reservoir on days i and $i-1$ (mm.day^{-1}), respectively, δ_E is the delay time for infiltrated water to reach the epikarst (days), $Q^{K}_{SURF,i,j}$, $Q^{K}_{LAT,i,j}$ and $Q^{K}_{PERC,i,j}$ are surface runoff, soil lateral flow, and soil percolation on day i from the karst HRU j (mm.day^{-1}), respectively, $RECH_{M,i}$ and $RECH_{M,i-1}$ represent recharge by soil water percolation from non-karst HRUs to the matrix reservoir on days i and $i-1$ (mm.day^{-1}), respectively, δ_M is the delay time for infiltrated soil water to reach the matrix (days), $nhrus-K$ is the number of karst HRUs in the recharge area, $Q^{NK}_{PERC,i,j}$ is the soil water percolation on day i from the non-karst HRU j (mm.day^{-1}), $RECH_{C,i}$ is the recharge by soil lateral flow in non-karst HRUs and water losses from channels to the conduit reservoir on day i (mm.day^{-1}), $Q^{NK}_{LAT,i,j}$ is the soil lateral flow on day i from non-karst HRU j (mm.day^{-1}), $Q_{TLOSS,i}$ represents water losses from channels on day i (mm.day^{-1}), and $nhrus-NK$ is the number of non-karst HRUs in the recharge area.

Epikarst reservoir

$$\begin{cases} \dfrac{dE(t)}{dt} = RECH_E(t) - Q_{EM}(t) - Q_{EC}(t) \\ \dfrac{dE(t)}{dt} = RECH_E(t) - k_{EM}\left(\dfrac{E(t) - E_{min}}{L_{ref}}\right)^{\alpha_{EM}} - k_{EC}\left(\dfrac{E(t) - E_{min}}{L_{ref}}\right)^{\alpha_{EC}} \end{cases} \quad (4)$$

Matrix reservoir

$$\begin{cases} \dfrac{dM(t)}{dt} = RECH_M(t) + Q_{EM}(t) - Q_{MC}(t) - Q_{MS}(t) - Q^{M}_{PUMP}(t) \\ \dfrac{dM(t)}{dt} = RECH_M(t) + Q_{EM}(t) - k_{MC}\left(\dfrac{C(t) - M(t)}{L_{ref}}\right)^{\alpha_{MC}} - k_{MS}\left(\dfrac{M(t)}{L_{ref}}\right)^{\alpha_{MS}} - Q^{M}_{PUMP}(t) \end{cases} \quad (5)$$

Conduit reservoir

$$\begin{cases} \dfrac{dC(t)}{dt} = RECH_C(t) + Q_{EC}(t) + Q_{MC}(t) - Q_{CS}(t) - Q_{PUMP}^{C}(t) \\ \dfrac{dC(t)}{dt} = RECH_C(t) + Q_{EC}(t) + k_{MC}\left(\dfrac{C(t)-M(t)}{L_{ref}}\right)^{\alpha_{MC}} - k_{CS}\left(\dfrac{C(t)}{L_{ref}}\right)^{\alpha_{CS}} - Q_{PUMP}^{C}(t) \end{cases} \quad (6)$$

where E, M and C are the daily water levels of the epikarst, matrix and conduit reservoirs (mm), respectively, Q_{EM} and Q_{EC} are the discharge components from reservoir E to reservoir M and reservoir C (mm.day^{-1}), respectively, E_{min} is the minimum water level for the activation of the epikarst discharge function (mm), L_{ref} is a reference length for normalization of the water level of the reservoirs (mm), Q_{MC} is the matrix-conduit bidirectional exchange flow (mm.day^{-1}), Q_{MS} and Q_{CS} are the matrix and conduit discharge components into the spring (mm.day^{-1}), respectively, k_{EM}, k_{EC}, k_{MC}, k_{MS}, and k_{CS} are the specific discharge coefficients of the epikarst, matrix and conduit reservoirs (mm.day^{-1}), α_{EM}, α_{EC}, α_{MC}, α_{MS}, and α_{CS} are positive exponents (unitless), and Q_{PUMP}^{M} and Q_{PUMP}^{C} are the pumping rates from the matrix and conduit reservoirs (mm.day^{-1}), respectively.

$$Q_{STREAM,i} = Q_{SPRING,i} + Q_{SURF,i} = Q_{MS,i} + Q_{CS,i} + Q_{SURF,i} \quad (7)$$

where $Q_{STREAM,i}$ is the total discharge downstream the Las Hountas karst spring, $Q_{SPRING,i}$ is the spring flow contribution of the karst aquifer to streamflow (sum of the matrix outflow $Q_{MS,i}$ and conduit outflow $Q_{CS,i}$), and $Q_{SURF,i}$ is the contribution of surface runoff generated in non-karst areas of the catchment to streamflow on day i (all variables are expressed in mm.day^{-1}). The simulated streamflow hydrograph is given in m^3.s^{-1}.

2.3. The ISPEEKH model input data

2.3.1. Topography, land use, soil and lithology

The DEM of the Baget catchment was obtained from the US Geological Survey's Shuttle Radar Topography Mission files at 30–m spatial resolution (https://earthexplorer.usgs.gov/). The catchment altitude ranges from 502 to 1404 m a.m.s.l., and slopes vary between 10 to 30 %. A land-use/cover map of the catchment was extracted at 100−m resolution from Corine Land Cover (CLC) database (https://land.copernicus.eu/pan-european/corine-land-cover), available at the Pan-European level for years 1990, 2000, 2006, 2012 and 2018. The land-use trajectory approach was applied to examine land-use change in the catchment over the hydrological simulation period of 2006–2018. Six land-use categories were identified, with no interannual changes detected. The catchment is mainly covered by broad-leaved and coniferous forests (85 %), followed by pastures (8 %), moors and heathland (5 %), sparse transitional woodland-shrub (1 %) and agricultural lands (1 %). A soil map of the catchment was derived from the Food and Agriculture Organization (FAO) Digital Soil Map of the World at 1:5,000,000 scale (https://www.fao.org/soils-portal/soil-survey/soil-maps-and-databases/faounesco-soil-map-of-the-world/en/), and overlaid with a lithology map, to delineate karst and non-karst HRUs based on the catchment lithology, and to simulate the recharge from the karst and non-karst landforms to the E, M and C reservoirs following the karst groundwater module of ISPEEKH. The Baget catchment model was created using QSWAT + 2.0.3 in QGIS based on the input DEM, land-use and soil maps, slope characteristics, and outlet location. A total of 19 subbasins and 225 HRUs were defined, with 116 HRUs being karst and 109 non-karst. The total area of the karst HRUs represented 70 % of the catchment area while the non-karst HRUs accounted for 30%, and the HRUs delineation followed the areal distribution of the karst and non-karst regions in the catchment.

2.3.2. Meteorological variables

The meteorological variables required to conduct the hydrological simulations with ISPEEKH, using the Penman Monteith approach for evapotranspiration estimation, are daily precipitation, minimum and maximum air temperature, relative humidity, wind speed, and solar radiation. The precipitation datasets used in this study were retrieved from: (1) Saint Girons weather station (43°00′19″N; 01°06′25″E; 414 m a.m.s.l.), located 8.3 km from the Baget catchment outlet, (2) CPC and E-OBS gauge-based products, (3) SAFRAN, COMEPHORE, and ERA5-Land reanalysis products, and (4) IMERG-LR, PERSIANN-CDR, CHIRPS, and SM2RAIN-ASCAT satellite-based products. Additionally, the daily minimum and maximum air temperature, relative humidity, wind speed, and solar radiation data were obtained from SAFRAN. The data points of the different products used in this study are shown in **Fig. S1** of the Supplementary file.

The CPC precipitation dataset (Chen et al., 2008) is part of the products suite of the CPC Unified Precipitation Project, underway at the United States National Oceanic and Atmospheric Administration (NOAA) Climate Prediction Center (CPC). The dataset is constructed by interpolating the daily records from more than 30,000 gauge stations using the optimal interpolation (OI) objective analysis technique (Jiang et al., 2023), with a spatial coverage of 0.5° global land and a daily temporal resolution from 1979 to the present (Xie et al., 2007). The CPC data are available for download at https://psl.noaa.gov/data/gridded/data.cpc.globalprecip.html.

E-OBS (European Daily High-Resolution Observational Gridded Dataset; Haylock et al., 2008) is a land-only gridded daily observational dataset for precipitation and other atmospheric variables over Europe. This dataset is based on observations from the meteorological stations (22,600 stations, September 2022) provided by the National Meteorological and Hydrological Services (NMHSs) and other data-holding institutes across Europe (Cornes et al., 2018). The E-OBS dataset is delivered on regular latitude-longitude grids with spatial resolutions of 0.1° and 0.25° from 1950 to near present (June 2023), and is accessible through the European Climate Assessment & Dataset (ECA&D, https://www.ecad.eu/download/ensembles/download.php). E-OBS version 25.0e − 10 km spatial resolution was adopted in this study.

COMEPHORE (COmbinasion en vue de la Meilleure Estimation de la Précipitation HOraiRE; Tabary, 2007; Tabary et al., 2012) is an hourly reanalysis of surface precipitation accumulation over metropolitan France at 1-km spatial resolution, provided by the French weather forecasting agency Météo-France for years 1997–2022. The COMEPHORE precipitation estimates are obtained using the data from the French network of 24 radars and hourly and daily precipitation rain gauges (approximately 4200 rain gauges with a daily time step including approximately 1200 rain gauges with an hourly time step) (Fumière et al., 2020; Le Roy et al., 2020).

SAFRAN (Système d'Analyse Fournissant des Renseignements Adaptés à la Nivologie; Quintana-Seguí et al., 2008) is an hourly analysis system of atmospheric variables (precipitation, 2-meter air temperature and humidity, 10-meter wind speed, downward solar and infrared radiation, and cloudiness), from 1958 to present, provided by Météo-France for metropolitan France and Corsica at 8-km spatial resolution.

Estimates of the surface variables are derived over homogeneous climatic areas, determined based on topography, and refined with respect to nearby gauge-based observations using the optimal interpolation method. The analyses of temperature, humidity, wind speed, and cloud cover are carried out every 6 hours based on a first guess from the weather prediction model ARPEGE (Déqué et al., 1994) or the ECMWF archives. Precipitation is analyzed at daily time step with an initial guess inferred from climatological fields (Vidal et al., 2010). The analyzed variables are then interpolated at the hourly time step, where hourly precipitation distribution is inferred using the diurnal specific humidity cycle and separated between rainfall and snow using the 0.5 °C isotherm (Moucha et al., 2021). Solar and infrared radiation are estimated from the vertical profiles of temperature, humidity, and cloudiness, using a radiative transfer model (Ritter and Geleyn, 1992) due to the lack of observations for these two variables. Finally, all atmospheric variables are projected to an 8-km regular grid at the elevation of the grid cells in each homogeneous climatic zone, using the vertical profiles for each zone.

ERA5-Land (fifth generation European Centre for Medium-Range Weather Forecasts ECMW Reanalysis on global land surface; Hersbach et al., 2020; Muñoz-Sabater et al., 2021) is a spatially enhanced global dataset for the land component of the ERA5 reanalysis product, which is developed by ECMWF at 0.25° spatial resolution and hourly temporal resolution from 1950 onwards. The ERA5-Land dataset is obtained by forcing the HTESSEL land surface component (version Cy45r1 of the Integrated Forecasting System ISF) with low atmospheric meteorological fields from ERA5. Precipitation data in ERA5-Land are generated from ERA5 through a linear interpolation method based on a triangular mesh (Wu et al., 2023), reducing the spatial resolution to 0.10° (Muñoz-Sabater et al., 2021). The dataset is available from the Copernicus Climate data store (https://cds.climate.copernicus.eu/cdsapp#!/dataset/reanalysis-era5-land?tab=overview). In this study, the ERA5-Land hourly dataset was aggregated to obtain daily values.

IMERG (Integrated Multi-satellitE Retrievals for the Global Precipitation Measurement (GPM) mission; Huffman et al., 2019) is a precipitation product with 30-min temporal resolution, 0.1° spatial resolution, and 60° N–60° S full coverage. The product combines microwave precipitation estimates and microwave precipitation-calibrated infrared fields, including monthly surface precipitation gauge analyses to create research-level products. The Late-run version of the dataset (IMERG-LR), characterized by 14 h latency, was adopted in the study, and the product was accumulated to daily time scale (https://gpm.nasa.gov/data/directory).

PERSIANN-CDR (Precipitation Estimation from Remotely Sensed Information using Artificial Neural Networks- Climate Data Record; Ashouri et al., 2015) is a multi-satellite precipitation dataset that provides near-global precipitation information (60°N-60°S latitude and 0°–360° longitude) at 0.25° spatial resolution and daily temporal resolution, from 1983 to near present. The PERSIANN-CDR precipitation estimate is generated by processing the Gridded Satellite (GridSat-B1) infrared data using the PERSIANN algorithm, and by artificial neural network training using the National Center for Environmental Prediction (NCEP) Stage IV hourly precipitation data (Nguyen et al., 2018; Salmani-Dehaghi and Samani, 2021). The PERSIANN-CDR data are publicly available through the U.S. NOAA National Centers for Environmental Information (NCEI) at https://www.ncdc.noaa.gov/cdr/atmospheric/precipitation-persiann-cdr and the Centre for Hydrometeorology and Remote Sensing (CHRS) Data Portal at http://chrsdata.eng.uci.edu.

CHIRPS (Climate Hazards center InfraRed Precipitation with Station data) is a quasi-global precipitation dataset covering 50°S-50°N (and all longitudes). The dataset incorporates 0.05° resolution satellite imagery with in-situ station data in order to create a gridded daily rainfall time series spanning from 1981 to near present (Funk et al., 2015). The daily/0.05° CHIRPS V2.0 dataset was used in this study (https://data.chc.ucsb.edu/products/CHIRPS-2.0/global_daily/netcdf/).

SM2RAIN-ASCAT (Soil Moisture to Rain—Advanced SCATterometer V1.5) is a global scale daily rainfall product of 10-km spatial resolution, obtained by application of the SM2RAIN algorithm (Brocca et al., 2014, 2019) to the Advanced SCATterometer (ASCAT) satellite soil moisture data (Wagner et al., 2013). In fact, SM2RAIN algorithm allows to invert the soil water equation to infer rainfall from the variation of soil moisture The SM2RAIN-ASCAT used in this study spans the period of 2007–2022, available at (http://hydrology.irpi.cnr.it/download-area/sm2rain-data-sets/).

The CPC, E-OBS, ERA5-Land and IMERG-LR coarse precipitation datasets were downscaled to 1-km resolution by leveraging the statistical information from CHELSA (Climatologies at high resolution for the earth's land surface areas; Karger et al., 2017), a high-resolution (30 arc sec, ~1-km) global downscaled climate product hosted by the Swiss Federal Institute for Forest, Snow and Landscape Research WSL. It is based on a mechanistical statistical downscaling of global reanalysis data or global circulation model output, and includes climate layers for various time periods and variables. A triple collocation technique was then applied to merge the downscaled CPC and IMERG-LR datasets (Filippucci et al., 2024). The resulting high-resolution precipitation products were applied in the hydrological modeling of the Baget catchment (**Fig. S1** of the Supplementary file). Precipitation data that have been downscaled are indicated with '-ds' appended to each product name throughout the manuscript.

2.3.3. Streamflow data

Streamflow at gauging station B1 (Fig. 1), located 60 m downstream of the Las Hountas spring, is calculated from the stream water level measured at 30 min-interval by a float-type water-level sensor and the rating curves calibrated for this station by Mangin (1975). The daily streamflow data from 01/01/2006 to 31/12/2018 at station B1 were used to calibrate and validate ISPEEKH for each precipitation dataset. During this period, streamflow was measured continuously, and the daily discharge varied from 0.04 to 8.95 $m^3.s^{-1}$, with an average value of 0.45 $m^3.s^{-1}$.

2.4. Sensitivity analysis, parameter estimation, and uncertainty quantification methods for the ISPEEKH model

2.4.1. Parameter ESTimation Tool (PEST) followed by sensitivity analysis

For each precipitation dataset, ISPEEKH was set up to simulate the Baget catchment daily streamflow from 2006 to 2018, with a 2–year warm-up period (2006–2007), a 6–year calibration period (2008–2013), and a 5-year validation period (2014–2018). The models were calibrated with respect to daily streamflow measured at the gauging station B1. A preliminary manual calibration was first performed to determine the appropriate range values of the emptying exponents and discharge coefficients that not only optimize the simulated streamflow but also accurately represent the simulated water levels of the epikarst, matrix, and conduit reservoirs. This calibration process is required as the ISPEEKH model's ability to reproduce the dynamic behavior of water storage in these reservoirs is contingent upon these parameters. In particular, the model must capture the flow patterns of the conduit and matrix water storage. For the conduit storage, this includes a rapid rise in water levels, followed by a swift water transfer to the spring during the high-flow periods and an attenuated response with a gradual depletion during the low-recharge periods. In contrast, matrix water storage should exhibit lower variability with slower water transfer and reduced discharge to the spring. This manual calibration helps avoid unrealistic scenarios where certain parameter combinations lead to continuously increasing water levels in one or more reservoir even when the streamflow simulation appears satisfactory. Under this application, it was found that the value of the emptying exponents of the epikarst-to-conduit flow (α_{EC}) and conduit-to-spring flow (α_{CS}) must not exceed 2.5. The models were then calibrated automatically using the non-linear, model-independent parameter estimator PEST (Doherty, 2018). PEST

Table 1
Selected parameters, parameters description, and ranges for sensitivity analysis and calibration of the ISPEEKH model.

Parameter	Parameter description	Parameter range	Input file	Hydrological process
cn_pastg_f(*cn_a*; c *n_b*; *cn_c*; *cn_d*)	SCS runoff curve numbers for pastures	−20 % to +15 % (relative)	cntable.lum	Surface runoff
cn_wood_f(*cn_a*; c *n_b*; *cn_c*; *cn_d*)	SCS runoff curve numbers for broad-leaved and coniferous forests	−20 % to +15 % (relative)		
esco	Soil evaporation compensation factor	0.9–1	hydrology. hyd	Evapotranspiration
epco	Plant uptake compensation factor	0.9–1		
perco	Percolation coefficient	0–0.5	hydrology. hyd	Soil water fluxes
awc	Available water capacity (mm H2O.mm^{-1} soil) of the i^{th} soil layer	−60 % to +80 % (relative)	soils.sol	
bd	Moist bulk density (g.cm^{-3} or Mg.m^{-3}) of the i^{th} soil layer	−20 % to +20 % (relative)	soils.sol	
sol_k	Saturated hydraulic conductivity (mm.h^{-1}) of the i^{th} soil layer	−20 % to +20 % (relative)	soils.sol	
$h_{E,0}$(*he_init*)	Initial water level in the epikarst (mm)	1–25	karst.data	Epikarst-matrix-conduit fluxes
E_{min}(*e_min*)	Minimum water level for epikarst flow activation	0.01–1		
δ_E(*gwdelay_e*)	Recharge delay to the epikarst (days)	0.5–2		
α_{EC}(*a_ec*)	Emptying exponent of the epikarst-conduit flow	0.5–2.5		
k_{EC}(*k_ec*)	Discharge coefficient of the epikarst-conduit flow (mm.day^{-1})	0.0001–0.095		
α_{EM}(*a_em*)	Emptying exponent of the epikarst-matrix flow	0.5–1.5		
k_{EM}(*k_em*)	Discharge coefficient of the epikarst-matrix flow	0.0001–0.01		
$h_{M,0}$(*hm_init*)	Initial water level in the matrix (mm)	1–25		
δ_M(*gwdelay_m*)	Recharge delay from the soil to the matrix (days)	1–3		
α_{MC}(*a_mc*)	Emptying exponent of the matrix-conduit flow	0.5–1.3		
k_{MC}(*k_mc*)	Discharge coefficient of the matrix-conduit flow (mm.day^{-1})	0.0001–0.05		
α_{MS}(*a_ms*)	Emptying exponent of the matrix-spring flow	0.5–1.5		
k_{MS}(*k_ms*)	Discharge coefficient of the matrix-spring flow (mm.day^{-1})	0.0001–0.01		
$h_{C,0}$(*hc_init*)	Initial water level in the conduit (mm)	1–25		
α_{CS}(*a_cs*)	Emptying exponent of the conduit-spring flow	0.5–2.5		
k_{CS}(*k_cs*)	Discharge coefficient of the conduit-spring flow (mm.day^{-1})	0.0001–0.095		

implements a local optimization technique that is based on the Gauss–Marquardt–Levenberg algorithm to minimize the objective function of the squared sum of weighted residuals between the simulated and observed data.

The Morris screening method (elementary-effects test) for qualitative global sensitivity analysis (GSA) (Morris, 1991) was applied to assess the sensitivity of the ISPEEKH model parameters governing streamflow. The selected parameters, which include those related to evapotranspiration, surface runoff, soil water fluxes, and karst groundwater fluxes, are listed in Table 1 with their respective value ranges for sensitivity analysis. The Morris method evaluates the relative sensitivity of the model parameters by calculating the change in the model output when a specific model parameter is altered (i.e., elementary effect), while keeping all other parameters constant. A single elementary effect for the *i*th parameter is computed as follows (Abbas et al., 2024):

$$EE_i = \frac{f(x_1, \cdots, x_i + \Delta_i, \cdots, x_p) - f(x)}{\Delta_i} \tag{8}$$

where EE_i is the elementary-effect value of the *i*th model parameter, f represents the model; $x_1, \cdots, x_i$ is the model parameter value, and Δ_i is the change in *i*th model parameter.

With this method, the mean and standard deviation of all elementary effects for a given model parameter are used to assess parameter sensitivity and are calculated as follows:

$$\mu_i^* = \frac{1}{n}\sum_{j=1}^{n} |EE_i(j)| \tag{9}$$

$$\sigma_i = \sqrt{\frac{1}{n-1}\sum_{j=1}^{n}\left[EE_i(j) - \frac{1}{n}\sum_{j=1}^{n} EE_i(j)\right]} \tag{10}$$

where μ_i^* and σ_i represent the mean and standard deviation of all EE_i for a given parameter *i*, and n is the number of EE_i computations.

The pestpp-sen software tool (White et al., 2020) within the PEST++ environment was implemented to generate parameter values, update ISPEEKH files, run the model simulations and compute sensitivity indices for the Morris method.

SWAT+ allows for the calibration of various parameters by applying a single value within a given parameter range, adding an increment to an existing value, or applying a relative change of spatial parameters. For the calibration of ISPEEKH with PEST, template files were created from the model input files by replacing the original values of the targeted calibration parameters in their respective input files with placeholders. Using these template files, the updated values of the calibration parameters are written to the model input files at each iteration of a PEST run. The parameters associated with the epikarst, matrix, and conduits reservoirs in the "karst.data" input file (i.e., initial reservoir water levels, infiltration delay times, threshold water level for flow activation, emptying exponents and discharge coefficients) correspond to the karst aquifer properties and are independent of the spatial variability of the surface HRUs. The curve numbers, evapotranspiration parameters, and soil parameters are calibrated at HRU level using template files of the "cntable.lum", "hydrology.hyd" and "soil.sol" input files, respectively.

2.4.2. *Iterative ensemble smoother (iES) for parameter estimation and uncertainty quantification*

The Iterative Ensemble Smoother (iES) method (Chen and Oliver, 2013), integrated in the pestpp-ies tool (White, 2018) within the PEST++ environment (Welter et al., 2015), was implemented in this study to generate prior (uncalibrated results) and posterior uncertainty estimates of ISPEEKH parameters. The iES method uses the Ensemble Kalman Filter (EnKF), an algorithm for data assimilation that updates state variables by incorporating measured data into the model results, based on correlations between the state variables and measured data (Evensen, 1994). The EnKF was initially implemented in the ensemble smoother scheme (ES) (Van Leeuwen and Evensen, 1996). ES was then modified by Chen and Oliver (2013) to operate iteratively using the Gauss–Levenberg–Marquardt (GLM) algorithm (the iES method) with a Jacobian matrix filled with finite-difference approximated derivatives, and to improve the minimization of the sum-of-squared residuals objective function for nonlinear problems. Chen and Oliver (2013) later

reformulated the GLM algorithm to derive an approximate Jacobian matrix empirically from an ensemble of random parameter values, whereby the model needs to be run once for each member of the ensemble (i.e. realization) rather than once for each parameter. This reformulation reduced the computational burden of populating a full rank Jacobian matrix for models with a large number of parameters while maintaining the ability to be parallelized and model independent (non-intrusive).

The iES method starts with a prior ensemble of parameter values. A Jacobian matrix of parameter sensitivities is derived from the relationships between the model parameters and output, using a range of parameter values from the prior ensemble. The Jacobian matrix is applied to update each parameter ensemble iteratively by minimizing model residuals through the GLM algorithm, resulting in a posterior ensemble of optimized model parameters. The propagation of the ensemble of parameter realizations until a satisfactory fit with the observed data yields an estimate of the posterior parameter distribution, which can be used to quantify the uncertainty in the forecasts of interest.

2.5. Model predictive performance evaluation

The capacity of the model to predict streamflow under the different precipitation datasets was evaluated with performance metrics commonly used in karst hydrology: the Nash-Sutcliff efficiency NSE (Nash and Sutcliffe, 1970), the coefficient of determination R^2, the percent of bias PBIAS (Gupta et al., 1999) (positive values indicate model underestimation bias, while negative values indicate model overestimation bias), and the Kling-Gupta efficiency KGE (Gupta et al., 2009), adopting the performance quality classes by Moriasi et al. (2015) and Jeannin et al. (2021). The non-parametric Kling-Gupta efficiency KGENP (Pool et al., 2018) and the correlation coefficients of Pearson *Rp* and Spearman *Rs* evaluation metrics were also computed so as to account for additional aspects of the model performance.

A wavelet multiresolution analysis (MRA), which is commonly used to decompose a signal into a progression of successive approximations and details in increasing order of resolution, was conducted to project streamflow on an orthogonal basis of wavelet generated from a filter band following a dyadic scale. For an orthogonal decomposition, the sum of all components returns the initial signal. The usual performance criteria consider the mean errors and do not capture how the model errors can be structured in time and frequency (Labat et al., 2000b; Sivelle et al., 2022). Thus, the application of MRA on both observed and simulated streamflow times series under the uncorrected and corrected precipitation datasets allows the evaluation of the hydrological model performance across different temporal scales by calculating the Pearson correlation coefficient (*Rp*) on the calibration and validation periods according to the dyadic scale.

2.6. Correction of the precipitation datasets

The preliminary assessment of the Baget catchment water balance conducted by Al Khoury et al. (2023) suggests that precipitation is generally underestimated in the study area, which results in the underestimation of the simulated streamflow. Several approaches are reported in the literature to correct the bias of precipitation products based on observed precipitation data from representative meteorological stations, including the ratio bias and dual-core smoothing correction methods, and the cokriging, probability matching, Bayesian correction, and optimal interpolation–probability matching methods, among others (Ye et al., 2023). In the case of the Baget catchment, the only available observed precipitation dataset is from the meteorological station of Saint Girons (414 m m.a.s.l), which is located outside the catchment at 8.3 km from its outlet. Therefore, in the absence of a precipitation monitoring network that captures the altitude effect within the catchment, the 1-km resolution COMEPHORE, CPC-ds, E-OBS-ds, ERA5-Land-ds, IMERG-LR-ds and merged CPC-IMERG-LR-ds gridded precipitation datasets were corrected in order to resolve the water balance discrepancy prior to model calibration by "Doing Hydrology Backward (DHB) (Kirchner's methodology). Accordingly, an orographic correction multiplicative factor (OCF_m) was computed for each dataset based on a rearranged water balance equation (Khan and Koch, 2018):

$$OCF_{m,i} = \frac{PCP_{true,i}}{PCP_{obs,i}} = \frac{Q_{obs} + ET_a - \Delta g}{P_{obs,i}} \quad (11)$$

where $OCF_{m,i}$ is the calculated orographic correction multiplicative factor for the gridded precipitation dataset *i*, Q_{obs} is the mean annual catchment discharge, ET_a is the catchment mean annual actual-evapotranspiration, Δg represents the catchment mean annual change in glacier storage, $P_{obs,i}$ is the observed (uncorrected) precipitation dataset *i*, and $PCP_{corrected,i}$ is the true (corrected) precipitation dataset *i*. The measured streamflow data at the gauging station B1 and the grid-based actual evapotranspiration estimates from SAFRAN over the 2006–2018 simulation period were used for the calculation of the OCF_m for each precipitation dataset (Table 2), and the change of glacier ice volume is null for the catchment.

Table 2
The orographic correction multiplicative factors (OCF_m) calculated for the 1-km resolution COMEPHORE, CPC-ds, E-OBS-ds, ERA5-Land-ds, IMERG-LR-ds and merged CPC-IMERG-LR-ds gridded precipitation datasets.

Precipitation dataset	OCF_m value
CPC-ds	2.03
E-OBS-ds	1.85
COMEPHORE	1.42
ERA5-Land-ds	1.23
IMERG-LR-ds	1.48
CPC-IMERG-LR-ds	1.89

3. Results and discussion

3.1. ISPEEKH parameters sensitivities under the precipitation products

The sensitivities of the selected parameters were computed under all precipitation datasets using the Morris screening method for minimizing streamflow errors. The sensitivity measures (i.e., the mean (μ^*) and the standard deviation (σ)) are based on the elementary effect absolute values of the model parameters and are not related to the scale and magnitude of the input or outputs. Thus, they show the relative relation between parameters (Abbas et al., 2024). The order of magnitude of (μ^*) and (σ) for all parameters and parameter sensitivity ranks remained consistent across all precipitation datasets, and the average values of (μ^*) and (σ) obtained from the sensitivity analysis run under each precipitation dataset are illustrated in Fig. 3. The discharge coefficient and emptying exponent of the conduit-to-spring flow (k_{CS};α_{CS}) and the discharge coefficient and emptying exponent of the epikarst-to-conduit flow (k_{EC};α_{EC}) ranked consistently as the top four most sensitive parameters irrespective of the input precipitation data, while the emptying exponents of the epikarst-to-matrix, matrix-to-spring, and bidirectional matrix-to-conduit fluxes (α_{EM};α_{MS};α_{MC}) were noticeably less sensitive than their counterparts α_{EC} and α_{CS}. This outcome is compatible with the discharge characteristics of the Baget catchment, which includes a shallow epikarst with high connectivity to a network of well-developed conduits in the saturated zone, resulting in most infiltration water passing from the epikarst to the conduits and emerging at the spring outlet , with a low contribution from the matrix to the overall discharge. The discharge coefficients of the epikarst-to-matrix flow, matrix-to-conduit bidirectional flow, and matrix-to-spring flow (k_{EM};k_{MC};k_{MS}) also ranked among the most sensitive parameters along with soil parameters (i.e., percolation coefficient *perco*, available water capacity

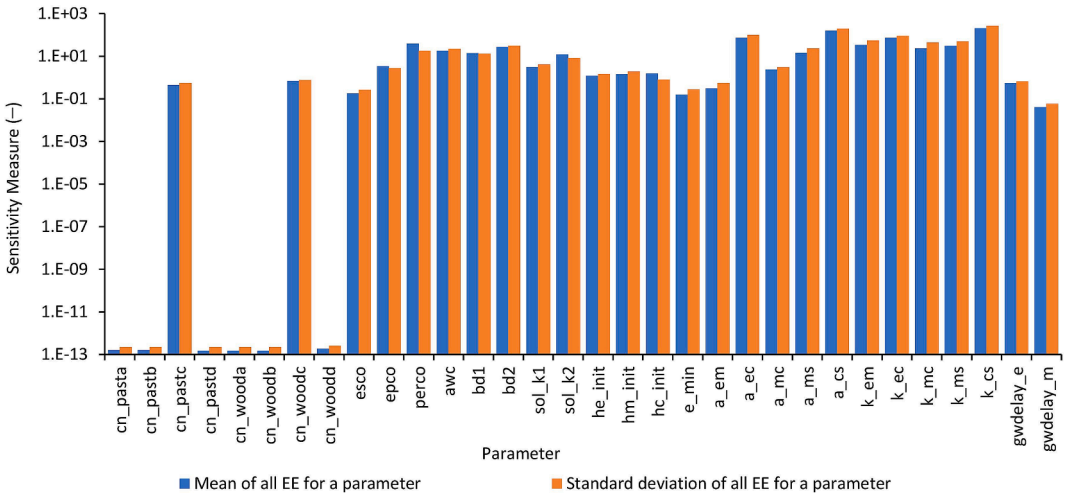

Fig. 3. Average values of the elementary effects (EE) mean (μ^*) and standard deviation (σ), calculated with the Morris global sensitivity analysis for the selected parameters of ISPEEKH with different precipitation datasets.

Table 3
Mean annual water balance in the Baget catchment (mm.year^{-1}) for years 2008 – 2018, simulated using ISPEEKH with Saint Girons gauge precipitation, gauge-based precipitation products (CPC, E-OBS), reanalysis products (SAFRAN, COMEPHORE and ERA5-Land), and satellite precipitation products (PERSIANN-CRD, IMERG-LR, CHIRPS, SM2RAIN-ASCAT). *PCP*: precipitation; *PET*: potential evapotranspiration, ET_a: actual evapotranspiration; *SURQ*: surface runoff; *RECH*: groundwater recharge; Q_{SPRING}: spring flow; Q_{STREAM}: streamflow.

Precipitation dataset	*PCP*	*PET*	ET_a	Q_{SURF}	*RECH*	Q_{SPRING}	Q_{STREAM}
Saint Girons	996.36	851.20	720.63	25.53	233.01	232.65	261.73
CPC	886.67	690.64	581.44	19.89	271.36	271.04	293.93
CPC-ds	892.17	686.97	581.87	26.47	265.76	265.43	295.25
E-OBS	949.78	681.60	574.54	44.54	311.30	311.17	360.01
E-OBS-ds	964.98	687.11	584.63	46.03	313.91	313.81	364.42
SAFRAN	1274.09	690.13	599.31	97.14	540.02	540.16	645.29
COMEPHORE	1287.34	686.84	591.07	132.54	517.80	517.49	660.00
ERA5-Land	1414.97	689.23	620.93	127.48	624.50	624.34	762.96
ERA5-Land-ds	1450.54	685.20	619.58	138.76	651.18	650.99	802.34
PERSIANN-CDR	982.77	692.03	598.29	30.75	341.02	340.66	375.64
IMERG-LR	1202.27	683.79	601.09	75.36	503.45	502.66	585.60
IMERG-LR-ds	1214.14	688.95	607.15	75.39	507.47	506.47	589.30
CPC-IMERG-LR-ds	950.85	687.30	596.73	37.34	296.66	296.36	337.57
CHIRPS	1098.07	695.29	597.00	53.94	441.35	441.45	502.13
SM2RAIN-ASCAT	1180.72	693.38	620.11	66.06	453.84	453.82	526.35

awc, and moist bulk density *bd*). Overall, the parameters governing karst groundwater flow and infiltration were the most sensitive while all surface runoff and evapotranspiration parameters ranked among the least sensitive. These results are also consistent with the recharge-discharge characteristics of the Baget catchment, where direct infiltration of most rainfall over the surface-exposed and well-developed epikarst zone feeds the karst aquifer and spring flow, with low surface runoff generation and contribution to the catchment streamflow.

Table 4
Daily streamflow statistical performance for the ISPEEKH model simulations driven by different precipitation datasets.

	Calibration				Validation			
Precipitation dataset	NSE	R^2	PBIAS	KGE	NSE	R^2	PBIAS	KGE
Saint Girons	−0.162	0.202	81.54 %	−0.226	0.171	0.46	72.17 %	0.016
CPC	−0.149	0.217	79.46 %	−0.223	0.106	0.469	68.53 %	−0.044
CPC-ds	−0.103	0.266	78.2 %	−0.179	0.101	0.474	69.7 %	−0.057
E-OBS	0.021	0.345	72.91 %	−0.064	0.278	0.537	63.67 %	0.109
E-OBS-ds	0.049	0.351	71.36 %	−0.034	0.268	0.525	64.62 %	0.101
SAFRAN	0.478	0.606	44.15 %	0.366	0.557	0.732	43.25 %	0.356
COMEPHORE	0.496	0.63	47.76 %	0.374	0.625	0.682	36.35 %	0.547
ERA5-Land	0.434	0.556	35.09 %	0.338	0.452	0.585	31.6 %	0.334
ERA5-Land-ds	0.459	0.555	32.06 %	0.379	0.477	0.577	27.72 %	0.379
PERSIANN-CDR	−0.127	0.113	67.87 %	−0.221	−0.102	0.098	66.52 %	−0.25
IMERG-LR	−0.018	0.114	51.36 %	−0.051	0.111	0.201	46.15 %	0.083
IMERG-LR-ds	−0.015	0.126	53.25 %	−0.062	0.094	0.174	43.29 %	0.088
CPC-IMERG-LR-ds	−0.047	0.296	74.8 %	−0.127	0.176	0.481	65.7 %	0.021
CHIRPS	0.058	0.201	53.53 %	0.030	−0.089	0.064	59.50 %	−0.177
SM2RAIN-ASCAT	0.024	0.255	59.08 %	−0.065	0.001	0.168	48.39 %	−0.105

3.2. Performance of the coarse and downscaled precipitation datasets for catchment water balance and streamflow simulation

The assessment of the Baget catchment water balance for the 2008–2018 period revealed that water balance is in deficit under all the precipitation data series (Table 3). The mean annual precipitation (*PCP*) varied between 887 mm under coarse CPC and 1451 mm under ERA5-Land-ds. The mean annual simulated streamflow (Q_{STREAM}) values ranged from 262 to 802 mm compared to a mean annual observed streamflow of 1145 mm in years 2008–2018. The simulated mean annual recharge (*RECH*) to the karst aquifer reservoirs was consistently equal to the simulated spring flow (Q_{SPRING}), showing that ISPEEKH modeled karst groundwater storage and spring flow from the recharge input successfully by conserving the water balance. The Baget is a conservative catchment with a groundwater recharge zone of 13.25 km^2 (Mangin, 1975), ruling out the possibility of additional water contribution to the spring discharge from a larger recharge area or interbasin groundwater flow. The Q_{SPRING} contribution to Q_{STREAM} varied between 80 and 92 %, while direct surface runoff (Q_{SURF}) accounted for the remaining 18–20 %, which is consistent with the Baget catchment discharge characteristics where the perennial Las Hountas karst spring is the primary source of discharge. The simulated mean actual evapotranspiration (ET_a) values (582–721 mm.$year^{-1}$) were comparable to the SAFRAN-based mean annual ET_a (667 mm), indicating that the uncertainty due to *ET* estimation is unlikely to generate the water balance discrepancy. Moreover, historical records also show that streamflow magnitude has been in the order of 1000 mm.$year^{-1}$ over the 1969–2005 period, indicating that the streamflow measurement uncertainty does not justify the water balance discrepancy. Thus, precipitation recorded at low altitude at Saint Girons station (414 m. a.m.s.l.), 8.3 km from the catchment outlet, cannot sustain the observed streamflow, while field observations in the 1973–1999 period report a mean annual precipitation of 1750 mm 0.5 km from the catchment (658 m a.m.s.l.) (Johannet et al., 2008).

Subsequently, the values of the NSE, R^2, and PBIAS metrics (Table 4) showed unsatisfactory performance for daily streamflow simulation (NSE $\leq$ 0.5, $R^2 \leq$ 0.6, PBIAS $\geq \pm$ 15 % in both calibration and validation periods (Moriasi et al., 2015). The SAFRAN and COMEPHORE reanalysis products, with mean annual *PCP* of 1274 and 1287 mm, respectively, scored higher NSE and R^2 values than all remaining precipitation products, particularly during validation where NSE and R^2 were satisfactory (0.50 < NSE $\leq$ 0.70; 0.60 < $R^2 \leq$ 0.75) despite a PBIAS of 40 %. The coarse and downscaled ERA5-Land datasets yielded the lowest PBIAS values (28 to 35 %) for streamflow underestimation among all precipitation products. In contrast, the performance from the gauge-based and satellite-based precipitation products was unacceptable, with NSE and KGE values close to or below 0, low R^2, and high PBIAS of 50 to 80 %. The reanalysis COMEPHORE, SAFRAN, and ERA5-Land precipitation products outperformed the gauge- and satellite-based precipitation products. Moreover, the spatial downscaling of the CPC, IMERG-LR, and E-OBS data to 1-km resolution and merging of the downscaled IMERG-LR and CPC data did not improve the predictive performance compared with the coarse datasets, while downscaling of ERA5-Land only improved the water balance estimation marginally by reducing the underestimation bias by 3–4 % across both the calibration and validation periods. The observed and simulated hydrographs under the ensemble of precipitation products are provided in Figs. S2–S6 of the Supplementary file**.** Overall, considerable discrepancies in the average annual precipitation estimates, exceeding 500 mm.$year^{-1}$, were revealed between the products. Hence, the reanalysis, gauge- and satellite-based precipitation products considered in this study do not represent the precipitation regime of the Baget catchment. Precipitation is generally underestimated in the Pyrenees region due to precipitation under catch by the rain gauges and the low-quality radar coverage in the mountainous regions, which corroborates the poor model predictive performance with the gauge- and satellite-based precipitation products.

Table 5
Optimal values of the emptying exponents (alpha) of the epikarst, matrix and conduit fluxes simulated by ISPEEKH under different precipitation datasets.

Precipitation dataset	α_{EM}	α_{EC}	α_{MC}	α_{MS}	α_{CS}
Saint Girons	1.000	2.500	1.129	0.519	2.201
CPC	0.863	2.484	1.055	0.512	2.466
CPC-ds	0.738	2.433	1.300	0.543	2.452
E-OBS	0.867	2.468	1.025	0.506	2.467
E-OBS-ds	0.920	2.474	1.085	0.506	2.462
SAFRAN	0.799	2.500	1.176	0.578	1.536
COMEPHORE	0.789	2.430	1.056	0.513	1.885
ERA5-Land	0.721	2.500	1.061	0.575	2.077
ERA5-Land-ds	0.734	2.500	0.939	0.570	1.985
PERSIANN-CDR	0.738	1.929	1.094	0.575	1.737
IMERG-LR	0.757	1.775	1.070	0.593	1.776
IMERG-LR-ds	0.743	1.788	1.032	0.585	1.920
CPC-IMERG-LR-ds	0.923	2.487	1.124	0.519	2.491
CHIRPS	0.764	1.918	1.033	0.584	1.933
SM2RAIN-ASCAT	0.820	2.455	1.033	0.503	2.500
Min	0.721	1.775	0.939	0.503	1.536
Max	1.000	2.500	1.300	0.593	2.500
Mean	0.812	2.309	1.081	0.545	2.126

Yet, the French kilometric dataset COMEPHORE benefits from rain gauge data collected by the French electricity company, which maintains various hydroelectric power plants to increase the quality of the dataset in several regions, such as Normandy and central France. The combination of radar and rainfall data in COMEPHORE provides a dataset on the Pyrenees that is of lower quality than the data on the rest of France but remains of higher quality than other observational precipitation databases currently available for this mountainous region (Fumière et al., 2020). This could justify the higher streamflow simulation performance obtained under COMEPHORE precipitation compared to the gauge- and satellite-based precipitation products. The results of our study could not be compared to those of previous studies in karst catchments, particularly those conducted by Mo et al. (2020), Mo et al. (2022) in the XiaJia (799.2 km^2) and Chengbi (2,087 km^2) karst river basins in China, due to the discrepancy in the basins' sizes relative to the Baget catchment (13.25 km^2) as well as the differences in the climatic features, landscape properties (i.e., topography, karst terrains, land use, and soil), and karst recharge and groundwater flow dynamics. Nonetheless, both studies reported an underestimation of flow under the raw IMERG satellite precipitation and underlined the need to apply correction and fusion methods based on gauge-measured precipitation to improve the model predictive performance.

The optimal values of the emptying exponents (alpha) of the epikarst, matrix and conduit fluxes are summarized in Table 5. The values of the epikarst-to-conduit flow emptying exponent α_{EC} (1.775–2.5; Mean: 2.309) and conduit-to-spring flow emptying exponent α_{CS} (1.536–2.5; Mean: 2.126) indicate that ISPEEKH simulated the conduit fluxes in the Baget catchment as non-linear, which is consistent with the karst aquifer discharge dynamics. These results indicate that the model is well adapted to reproduce the hydrodynamic behavior of the study catchment, despite underestimating streamflow under all precipitation products. On the other hand, the emptying exponent of the matrix-to-conduit bidirectional flow rate α_{MC} (0.939–1.3; Mean: 1.081) was mostly close to 1, suggesting that the exchange flow between the conduit and the surrounding matrix is primarily determined by the hydraulic conductivity of the fissured system.

3.3. Performance of the corrected and downscaled precipitation datasets for catchment water balance and streamflow simulation

Following the correction of the COMEPHORE, CPC-ds, E-OBS-ds, ERA5-Land-ds, IMERG-LR-ds and merged CPC-IMERG-LR-ds precipitation data, the calibrated ISPEEKH models yielded comparable values of the water balance components for the 2008–2018 period, with mean annual *PCP* of 1781–1824 mm, ET_a of 598–620 mm (equivalent to

Table 6
Mean annual water balance fluxes in the Baget catchment (mm.year^{-1}) for years for 2008 – 2018, simulated using ISPEEKH with the corrected precipitation datasets of the 1-km resolution COMEPHORE and downscaled CPC, E-OBS, ERA5-Land, IMERG-LR, and CPC-IMERG-LR products.

Precipitation dataset	*PCP*	*PET*	ET_a	Q_{SURF}	*RECH*	Q_{SPRING}	Q_{STREAM}
CPC-ds	1801.51	684.69	608.15	224.41	919.75	919.47	1164.76
E-OBS-ds	1788.33	685.09	602.63	210.29	963.24	962.91	1193.82
COMEPHORE	1823.76	685.15	598.35	236.71	926.39	926.24	1184.05
ERA5-Land-ds	1780.99	684.39	620.16	207.46	933.96	932.08	1159.57
IMERG-LR-ds	1792.90	688.06	619.85	193.71	951.99	949.33	1162.39
CPC-IMERG-LR-ds	1799.23	685.19	617.59	208.93	944.92	944.48	1173.16

Table 7
Daily streamflow statistical performance indices for the ISPEEKH simulations driven by the corrected COMEPHORE and downscaled ERA5-Land, CPC, E-OBS, IMERG-LR, and merged CPC-IMERG-LR precipitation datasets.

	Calibration				Validation			
Precipitation dataset	NSE	R^2	PBIAS	KGE	NSE	R^2	PBIAS	KGE
CPC-ds(1)	0.638	0.65	2.58 %	0.787	0.533	0.54	−6.33 %	0.666
CPC-ds(2)	−0.103	0.266	78.2 %	−0.179	0.101	0.474	69.7 %	−0.057
E-OBS-ds(1)	0.646	0.666	−2.25 %	0.81	0.67	0.66	−6.23 %	0.786
E-OBS-ds(2)	0.049	0.351	71.36 %	−0.034	0.268	0.525	64.62 %	0.101
COMEPHORE(1)	0.719	0.736	3.20 %	0.854	0.637	0.732	−10.65 %	0.772
COMEPHORE(2)	0.496	0.63	47.76 %	0.374	0.625	0.682	36.35 %	0.547
ERA5-Land-ds(1)	0.56	0.564	1 %	0.603	0.523	0.531	−4%	0.547
ERA5-Land-ds(2)	0.459	0.555	32.06 %	0.379	0.477	0.577	27.72 %	0.379
IMERG-LR-ds(1)	0.016	0.087	3.87 %	0.168	0.014	0.108	−7.37 %	0.232
IMERG-LR-ds(2)	−0.015	0.126	53.25 %	−0.062	0.094	0.174	43.29 %	0.088
CPC-IMERG-LR-ds(1)	0.623	0.624	2.1 %	0.719	0.499	0.503	−7.3 %	0.614
CPC-IMERG-LR-ds (2)	−0.047	0.296	74.8 %	−0.127	0.176	0.481	65.7 %	0.021

(1) precipitation dataset after correction.
(2) precipitation dataset before correction.

33–35 % of *PCP*), Q_{SURF} of 194–237 mm, *RECH* and Q_{SPRING} of 920–963 mm, and Q_{STREAM} of 1160–1194 mm (equivalent to 65–67 % of *PCP*) (Table 6). Q_{SPRING} represented 78–82 % of Q_{STREAM} and channel flow amounted to the remaining 18–22 %. The PBIAS (absolute values) were reduced considerably to less than 5 % in calibration and 10 % in validation after precipitation correction.

The corrected COMEPHORE precipitation yielded the streamflow simulation with the highest overall NSE, R^2, and KGE values (Table 7), indicating satisfactory ($0.50 < NSE \leq 0.70$; $0.60 < R^2 \leq 0.75$) to good performance ($0.70 < NSE \leq 0.80$; $0.75 < KGE \leq 0.85$) based on Moriasi et al. (2015) and Jeannin et al. (2021). The corrected E-OBS-ds precipitation improved the model predictive performance from unacceptable to satisfactory, both in calibration and validation. The CPC-ds and merged CPC-IMERG-LR-ds precipitation correction also enhanced the model performance, particularly in calibration where both NSE and R^2 surpassed 0.6 compared to 0.5 in validation, while KGE exceeded 0.7 in calibration and 0.6 in validation. On the other hand, the NSE and R^2 metrics varied only marginally under the corrected ERA5-Land-ds precipitation, as opposed to KGE increasing from 0.38 to above 0.6 and 0.5 in calibration and validation, respectively. Finally, the corrected IMERG-LR-ds precipitation consistently performed poorly in streamflow simulation, with very low NSE, R^2, and KGE metrics.

Although precipitation correction ensured water balance closure by mitigating the streamflow volume underestimation, this approach did not improve streamflow simulation for every precipitation dataset. The model driven by the corrected COMEPHORE precipitation best reproduced the discharge patterns during the high-flow periods by preserving the rising and recession of the observed hydrograph, while accurately estimating most peak flow values (Fig. 4**c**). In comparison, the models run with the corrected CPC-ds (Fig. 4**a**), E-OBS-ds (Fig. 4**b**) and merged CPC-IMERG-LR-ds (Fig. 4**f**) precipitation datasets often underestimated peaks greater than 3 $m^3.s^{-1}$. Moreover, the model better estimated flow during recession under the corrected COMEPHORE precipitation rather than the CPC-ds, EOBS-ds and merged CPC-IMERG-LR-ds precipitation. Under the corrected ERA5-Land-ds precipitation, peak flow rates were generally underestimated, while intermediate and low flows were overestimated, resulting in simulated falling limbs that are higher than the falling limbs of the observed hydrograph (Fig. 4**d**). Moreover, the simulated and observed hydrographs under the corrected IMERG-LR-ds precipitation were asynchronous and showed noticeable discrepancies for the high- and low-flow magnitudes (Fig. 4**e**). Nonetheless, the NSE, KGE, KGENP, Rp and Rs metrics, calculated for the mean simulated daily streamflow hydrographs and plotted in radar charts for the calibration and validation periods (Fig. 5), showed a globally higher model predictive performance under the ensemble of corrected precipitation data. Fig. 6 illustrates the observed and best estimated daily streamflow with prior and posterior prediction uncertainty bands under the corrected COMEPHORE precipitation. The plot in Fig. 6**a** represents the prior parameter ensembles with wider uncertainty bands, while the plot in Fig. 6**b** shows the posterior ensemble that reduced the uncertainty band, indicating that the ensemble smoother has incorporated the observational data effectively with higher quality precipitation data.

Fig. 7 shows the Pearson correlation coefficient (Rp) performance metric as a function of time scale, based on the application of an orthogonal wavelet decomposition on the observed and simulated streamflow under the uncorrected and corrected 1-km resolution precipitation datasets. The uncorrected COMEPHORE and ERA5-Land-ds reanalysis precipitation products had comparable performances and outperformed their counterparts for the various scales. Correlations under COMEPHORE ranged from 0.289 to 0.874 in the calibration period and 0.228 to 0.906 in the validation period for the 2- to 32-day scales, while correlations under ERA5-Land-ds varied from 0.098 (2 days) to 0.819 (32 days) in calibration and 0.156 (2 days) to 0.836 (16 days) in validation. The uncorrected CPC-ds and E-OBS-ds gauge-based precipitation datasets yielded correlations of 0.182–0.564 and 0.245–0.666, respectively, in calibration for the 2- to 32-day scales, and correlations of 0.262–0.767 and 0.198–0.827, respectively, in validation. Moreover, the uncorrected CPC-IMERG-LR-ds precipitation scored correlations in the range of 0.201 (2 days)–0.588 (32 days) during calibration and 0.401 (2 days)–0.804 (32 days) during validation. The

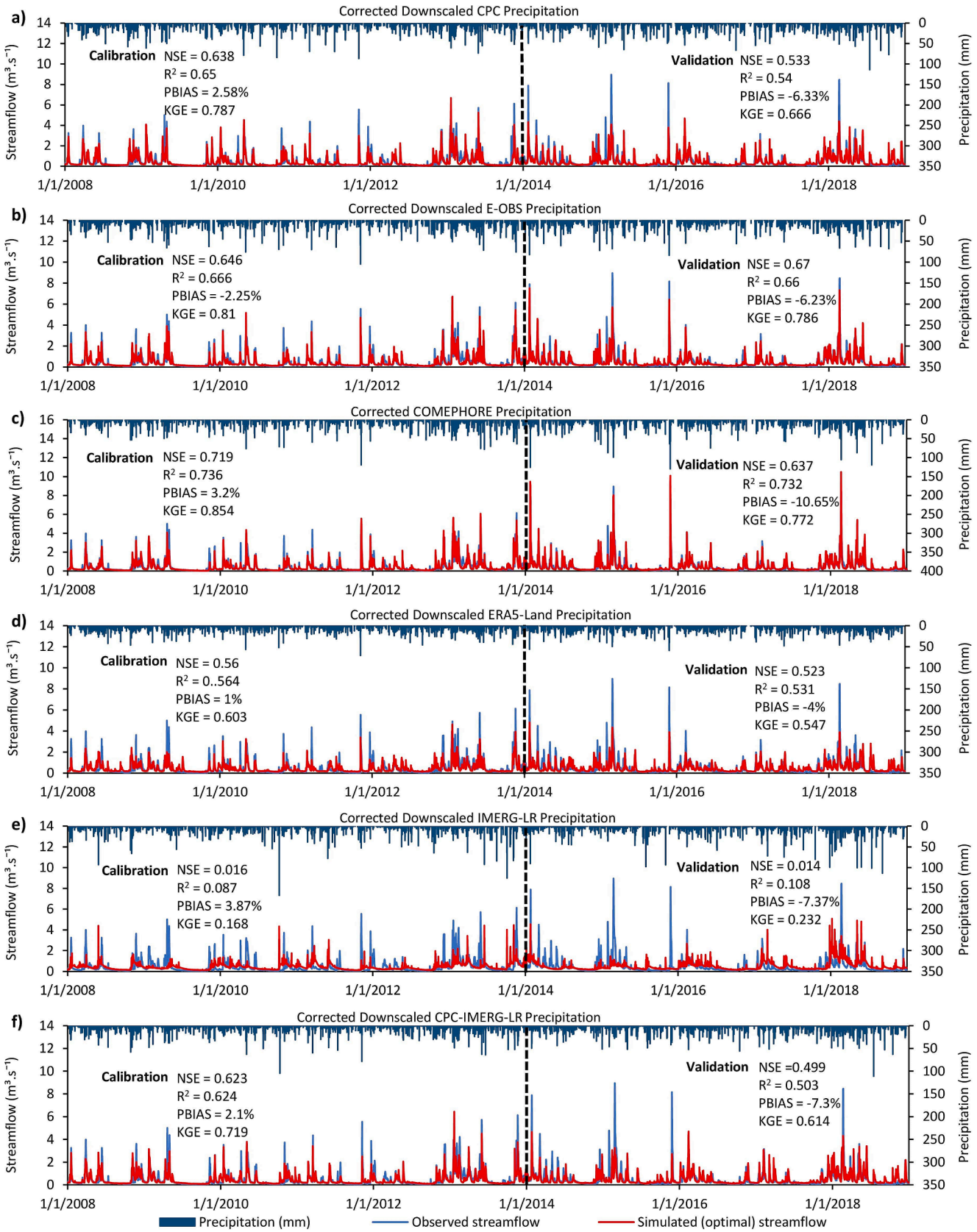

Fig. 4. Daily observed and simulated streamflow of the Baget catchment in years 2008–2018, using the ISPEEKH model driven by the corrected (a) downscaled CPC precipitation, (b) downscaled E-OBS precipitation, (c) COMEPHORE precipitation, (d) downscaled ERA5-Land precipitation, (e) downscaled IMERG-LR precipitation, and (f) downscaled merged CPC-IMERG-LR precipitation. NSE: Nash–Sutcliffe Efficiency; R^2: coefficient of determination; PBIAS: percent bias; KGE: Kling–Gupta Efficiency.

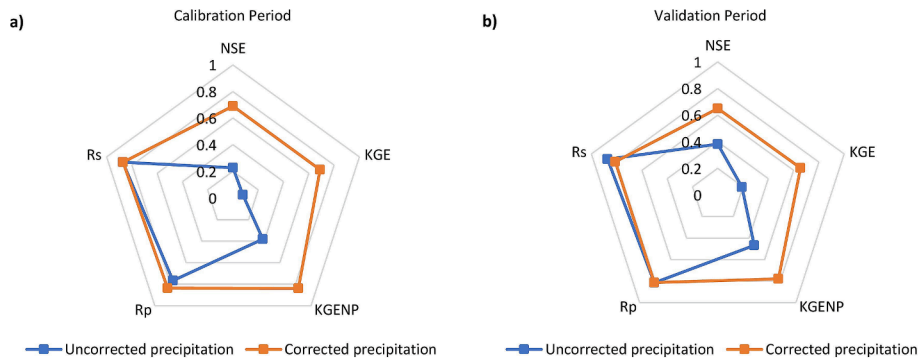

Fig. 5. Radar chart of the NSE (Nash-Sutcliffe Efficiency), KGE (Kling Gupta Efficiency), KGENP (Kling Gupta Efficiency Non-Parametric), Rp (Pearson correlation coefficient), and Rs (Spearman correlation coefficient) performance criteria for the (a) calibration and (b) validation periods of the mean daily streamflow ISPEEKH simulations with the uncorrected and corrected precipitation datasets.

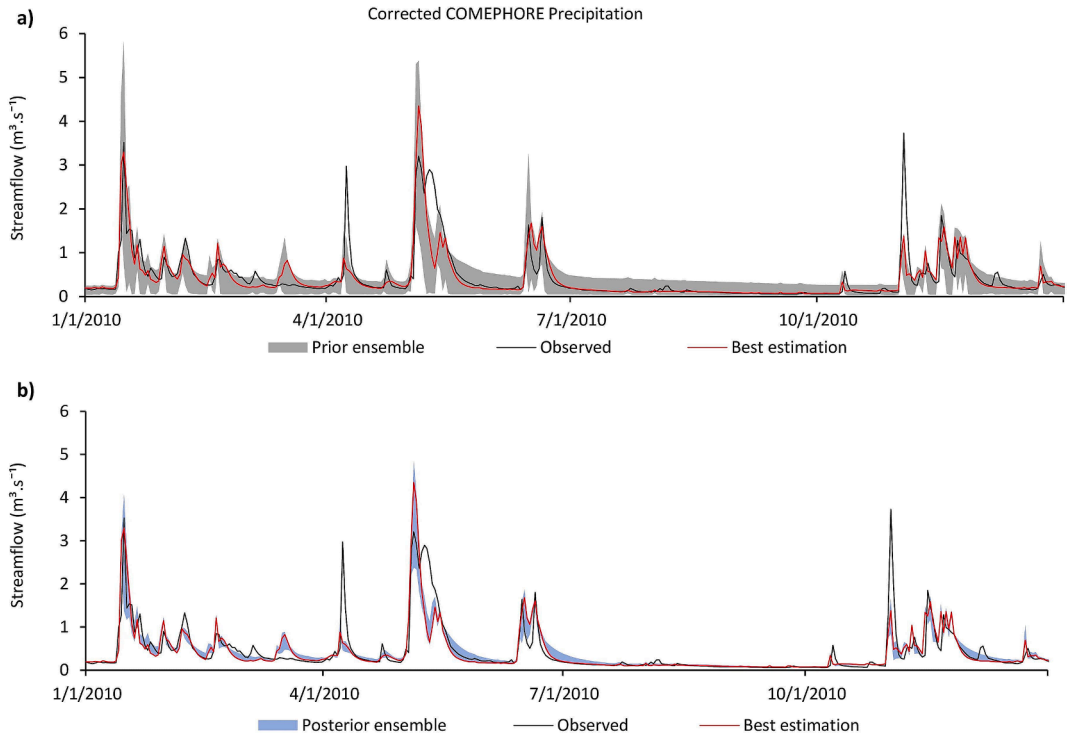

Fig. 6. (a) Prior and (b) posterior prediction uncertainty bands for streamflow simulation in the Baget catchment using ISPEEKH driven by corrected COMEPHORE precipitation dataset.

model driven by the uncorrected IMERG-LR-ds precipitation showed the poorest performances: correlations were negative for the 2-day scale, and varied from 0.132 (4 days) to 0.252 (32 days) in calibration and 0.16 (4 days) to 0.387 (16 days) in validation.

Model performance improved across the various time scales under the corrected COMEPHORE, E-OBS-ds, and CPC-ds products. The corrected COMEPHORE precipitation exhibited the highest correlations, which ranged from 0.785 to 0.941 in the calibration period and 0.769 to 0.931 in the validation period for the scales from 4 days to 32 days. Under the E-OBS-ds precipitation, correlations increased to 0.686 (4 days)–0.932 (32 days) in calibration and to 0.703 (4 days)–0.919 (32 days) in validation. Correlations also improved considerably under the corrected CPC-ds precipitation, increasing to 0.699–0.862 and 0.656–0.819 for the 4- to 32-day scales. On the other hand, correlations were higher with the CPC-IMERG-LR-ds precipitation mainly during calibration, increasing to 0.322 (2 days)–0.846 (32 days). Under the corrected ERA5-Land-ds precipitation, correlation values increased slightly (0.652–0.833) in the calibration period for the 4- to 32-day scales but decreased (0.031–0.741) in the validation period, showing an overall comparable model performance to the uncorrected ERA5-Land-ds precipitation. Correlations only increased in the calibration period for the 16- to 32-day scales but diminished in the validation period under the corrected IMERG-LR-ds precipitation, indicating a lower model performance compared to the uncorrected IMERG-LR-ds precipitation.

Fig. 8 shows the envelopes of monthly average simulated streamflow values under the various uncorrected and corrected 1-km resolution precipitation datasets. The envelope formed with the uncorrected precipitation data reveals significant discrepancies between simulated and observed discharge, at both monthly and annual scales. This suggests limitations in the ISPEEKH model's ability to accurately reproduce the catchment hydrological processes when driven with uncorrected precipitation inputs. In contrast, the envelope with corrected precipitation datasets demonstrates satisfactory predictive performances, with

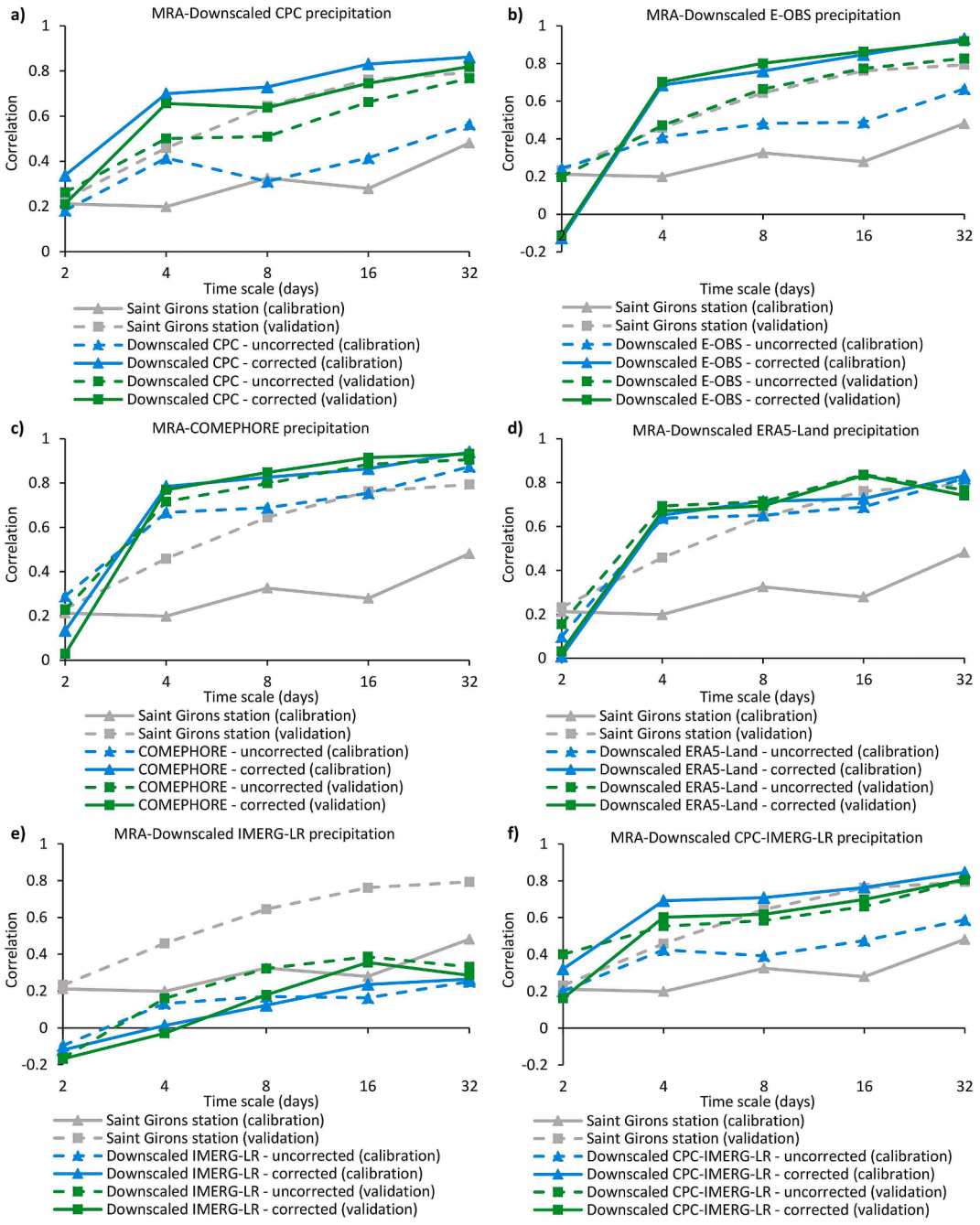

Fig. 7. Pearson correlation coefficient (Rp) performance criteria over the calibration and validation periods, based on an orthogonal wavelet decomposition of the observed and simulated streamflow times series under the uncorrected and corrected 1-km resolution precipitation datasets.

narrower ranges of simulated streamflow values and reduced discrepancies between the simulated and observed discharge patterns, both in the calibration and validation periods. Thus, the incorporation of corrected precipitation data has enhanced the reliability and predictive capability of the hydrological model, leading to more robust simulations of streamflow dynamics.

3.4. Study limitations and future perspectives

This study underscored the importance of accurate precipitation data quality for the hydrological modeling of mesoscale ungauged karst catchments characterized by quick-flow processes. It highlighted the value of applying corrected precipitation datasets at downscaled spatial resolution in order to enhance the hydrological model's predictive capability of streamflow in such catchments as opposed to relying on globally used gauge-based, satellite-based and reanalysis precipitation products at coarse spatial resolutions. A catchment-scale precipitation volume correction was performed to close the water budget before model calibration by "Doing Hydrology Backward (DHB)" (Kirchner's methodology), with orographic correction multiplicative factors calculated for the 1-km resolution precipitation products. This correction method, however, did not improve the simulated hydrographs under all precipitation datasets. The corrected COMEPHORE reanalysis product, specifically developed by merging radar and rain gauge data for metropolitan France, delivered the best simulation results, suggesting that fine-resolution regionally-tailored reanalysis precipitation products could serve as base data for streamflow simulation in remote meso-scale karst catchments.

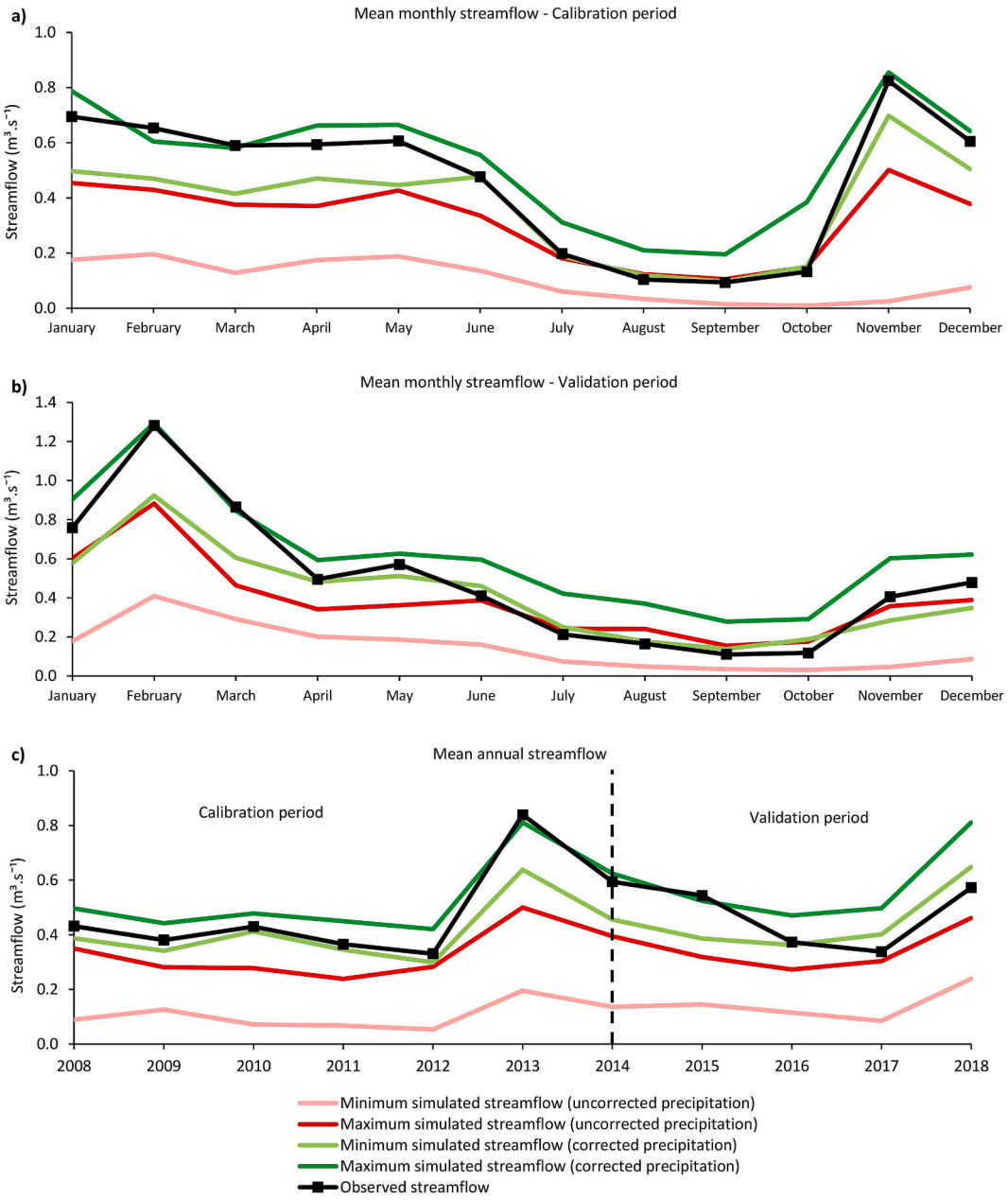

Fig. 8. Mean observed streamflow and mean minimum and maximum values of the ensemble of ISPEEKH streamflow simulations under the uncorrected and corrected precipitation datasets considering (a) the calibration period at monthly scale, (b) validation period at monthly scale, and (c) both calibration and validation periods at annual scale.

This finding underscores a critical limitation: the absence of representative precipitation gauges within the study catchment. Raw precipitation products, whether gauged-based, satellite-based or reanalysis, cannot fully substitute for direct, localized observations. Moreover, the bias correction of these products, while necessary, is insufficient to achieve high accuracy without a robust network of precipitation gauges within the catchment. The presence of such gauges is indispensable for capturing the spatial and temporal variability of precipitation, ensuring the reliability of hydrological models in similar ungauged or sparsely gauged regions. Thus, for future research, daily and subdaily operating rain gauges should be installed at different altitudes in the Baget catchment in order to capture the spatial and temporal distribution characteristics of the catchment precipitation, then evaluate the spatial and temporal scale accuracy of regional and global precipitation products with respect to the station-measured precipitation. Subsequently, different correction methods could be applied to these products, and watershed hydrological modeling could then be performed with the raw and corrected precipitation datasets so as to re-evaluate their accuracy at daily and subdaily time scales, and assess the performance of the correction methods.

Several approaches are reported in the literature to correct gridded precipitation products with gauge observations such as ratio bias correction, dual-core smoothing correction, Bayesian correction, cokriging, probability matching, optimal interpolation–probability matching, integrated fusion through inverse error variance weighting (Ye et al., 2023), artificial neural networks (Ait Dhmane et al., 2023), frequency correction (Li et al., 2023), and distribution mapping (Londhe et al., 2023). On the other hand, the elevation bands method has been commonly used in SWAT to consider the orographic effects on precipitation in mountainous regions. The method applies up to ten equally spaced elevation bands in each subbasin to adjust regional precipitation by weighting the elevation difference between the rain gauge and the

band, and multiplying the elevation difference by a constant input precipitation lapse rate (Tuo et al., 2016). Several studies have shown that the elevation bands method in SWAT enhanced the accuracy of the precipitation estimation and runoff simulations in mountainous regions (Chiphang et al., 2020; Wu et al., 2019; Zhang et al., 2015), while others underlined the need to improve it as the increase in precipitation with altitude should not be constant but rather dependent on the precipitation amount. In their study, Galván et al. (2014) observed that the elevation band method in SWAT often underestimates intense precipitation and overestimates lower precipitation due to discrepancies between subbasin altitudes and rain gauge elevations. To address this, they proposed a modification to the SWAT source code that calculates a ratio to multiply precipitation at the recording gauge and determine precipitation in the elevation band, rather than adding a constant value. Similarly, Grusson et al. (2015) identified issues with SWAT's overestimation of snow at higher elevations, attributed to the use of uniform temperature and precipitation lapse rates. They suggested two approaches to mitigate this limitation: (1) increasing the number of elevation bands, or (2) using the existing bands more effectively by setting thinner bands at higher altitudes to cover smaller elevation ranges. In SWAT+, the precipitation and temperature lapse rates should adjust precipitation and temperature based on elevation data from spatial objects and weather files. Although these changes were planned to be reflected in the SWAT+ source code and documentation, the new inputs were not operational in the version of SWAT+ used in this study.

Finally, continuous streamflow data from gauge station B1 was used to calibrate the model. However, since spring flow is a major component of streamflow in the Baget catchment, the absence of continuous spring flow measurements for calibration limits the model's ability to fully capture groundwater dynamics, introducing uncertainty in simulating both spring flow and overall streamflow. Therefore, future work should prioritize the collection of continuous spring flow data at Las Hountas, along with groundwater level measurements and hydrogeochemical data, to enable a more comprehensive model calibration. This would result in a more accurate representation of water fluxes and storage dynamics within the karst aquifer, ultimately improving streamflow predictions.

4. Conclusions

This study evaluated the performance of several coarse- and fine-resolution precipitation products in simulating daily streamflow in the small-scale Baget karst catchment (13.25 km^2), located in a sparsely monitored region in the Pyrenees mountains, southwest of France, and characterized by rapid rainwater infiltration. The ensemble of precipitation datasets used in this study included: the gauged-based products CPC and E-OBS, the reanalysis products SAFRAN, COMEPHORE and ERA5-Land, and the satellite-based products PERSIANN-CDR, IMERG-LR, SM2RAIN-ASCAT, and CHIRPS. The CPC, E-OBS, ERA5-Land, and IMERG-LR precipitation datasets were downscaled to 1-km resolution and applied together with 1-km resolution merged CPC-IMERG-LR precipitation in the hydrological analysis. The Baget catchment's hydrological response to the precipitation products was simulated over the years 2006–2018 using the ISPEEKH model, a modified variant of the Soil and Water Assessment Tool (SWAT+) for spring flow-dominated karst watersheds. This model incorporates three non-linear reservoirs to simulate fluxes of the epikarst, conduit, and matrix water-bearing components in a karst aquifer. In conclusion:

- The discharge coefficients and emptying exponents governing the epikarst outflow to the conduits and the conduit outflow to the spring were the most sensitive model parameters across the precipitation products used in this study. This result aligns with the discharge patterns observed in the Baget catchment, where fast recharge and conduit-dominated flow are prevalent.
- Water balance analysis from 2008 to 2018 revealed a noticeable deficit under the ensemble of the precipitation datasets. The gauge- and satellite-based precipitation products yielded the lowest model prediction performances, with a flow underestimation bias of around 48 to 74 %. The reanalysis products outperformed the gauge- and satellite-based precipitation products, scoring higher NSE, R^2, and KGE metrics, and an overall 30–44 % flow underestimation bias. The COMEPHORE precipitation performed best, followed by SAFRAN and ERA5-Land precipitation.
- The downscaling of the CPC, IMERG-LR, ERA5-Land and E-OBS precipitation datasets to finer 1-km spatial resolution improved the model predictive performance insubstantially or only marginally compared to the coarse datasets.
- The optimal values of the emptying exponents of the epikarst-to-conduit and conduit-to-spring outflows, simulated under the ensemble of the precipitation products, were mostly greater than 2, suggesting that ISPEEKH was adapted to reproduce the non-linear conduit flow dynamics in the Baget catchment and that the discrepancy in the model predictive performance is mainly related to precipitation quality.
- Finally, this study underscored the significance of incorporating spatially distributed and corrected precipitation from various products in order to enhance the reliability of models in the hydrological simulation of highly responsive small karst catchments. Based on catchment-scale precipitation correction, the COMEPHORE reanalysis of precipitation covering mainland France generated the best streamflow simulation, highlighting the need to install in-situ gauges stations at various altitudes in the catchment to correct the fine resolution reanalysis precipitation data for further improvement of the discharge simulations.

CRediT authorship contribution statement

Ibrahim Al Khoury: Writing – review & editing, Writing – original draft, Visualization, Software, Methodology, Formal analysis, Data curation, Conceptualization. **Laurie Boithias:** Writing – review & editing, Supervision, Project administration, Methodology, Formal analysis, Conceptualization. **Vianney Sivelle:** Writing – review & editing, Visualization, Methodology, Investigation, Formal analysis, Conceptualization. **Ryan T. Bailey:** Writing – review & editing, Visualization, Software, Methodology. **Salam A. Abbas:** Writing – review & editing, Visualization, Software, Methodology. **Paolo Filippucci:** Writing – review & editing, Methodology, Data curation. **Christian Massari:** Writing – review & editing, Methodology. **David Labat:** Writing – review & editing, Supervision, Project administration, Methodology, Funding acquisition, Formal analysis, Conceptualization.

Funding

This research has been supported through the grant EUR TESS N°ANR-18-EURE-0018 in the framework of the Programme des Investissements d'Avenir and the Ministry of Higher Education, Research and Innovation (Ministère de l'Enseignement Supérieur, de la Recherche et de l'Innovation, MESRI) of France.

Declaration of competing interest

The authors declare that they have no known competing financial interests or personal relationships that could have appeared to influence the work reported in this paper.

Acknowledgments

The authors would like to thank the KARST observatory network (SNO KARST) initiative at the INSU/CNRS, which aims to strengthen knowledge sharing and promote cross-disciplinary research on karst

systems at the national scale. We also thank Météo-France for providing meteorological data used in this study. We would also like to dedicate this contribution to the memory of Alain Mangin and his long-term invaluable care of collecting data on the Baget catchment. We acknowledge the E-OBS dataset from the EU-FP6 project UERRA (http://www.uerra.eu) and the Copernicus Climate Change Service, and the data providers in the ECA&D project (https://www.ecad.eu). We equally thank Météo-France for providing the meteorological data used in this study

Appendix A. Supplementary data

Supplementary data to this article can be found online at https://doi.org/10.1016/j.jhydrol.2024.132131.

Data availability

Data will be made available on request.

References

Abbas, S.A., Bailey, R.T., White, J.T., Arnold, J.G., White, M.J., Čerkasova, N., Gao, J., 2024. A framework for parameter estimation, sensitivity analysis, and uncertainty analysis for holistic hydrologic modeling using SWAT+. Hydrol. Earth Syst. Sci. 28, 21–48. https://doi.org/10.5194/hess-28-21-2024.

Ait Dhmane, L., Moustadraf, J., Rachdane, M., Saidi, M.E., Benjmel, K., Amraoui, F., Ezzaouini, M.A., Ait Sliman, A., Hadri, A., 2023. Spatiotemporal assessment and correction of gridded precipitation products in North Western Morocco. Atmosphere 14 (8), 1239. https://doi.org/10.3390/atmos14081239.

Al Khoury, I., Boithias, L., Bailey, R.T., Ollivier, C., Sivelle, V., Labat, D., 2023. Impact of land-use change on karst spring response by integration of surface processes in karst hydrology: The ISPEEKH model. J. Hydrol. 626, 130300. https://doi.org/10.1016/j.jhydrol.2023.130300.

An, L., Hao, Y., Yeh, T.-C.-J., Liu, Y., Liu, W., Zhang, B., 2020. Simulation of karst spring discharge using a combination of time–frequency analysis methods and long short-term memory neural networks. J. Hydrol. 589, 125320. https://doi.org/10.1016/j.jhydrol.2020.125320.

Arnaud, P., Lavabre, J., Fouchier, C., Diss, S., Javelle, P., 2011. Sensitivity of hydrological models to uncertainty in rainfall input. Hydrol. Sci. J. 56, 397–410. https://doi.org/10.1080/02626667.2011.563742.

Aryal, A., Tran, T.-N.-D., Kumar, B., Lakshmi, V., 2023. Evaluation of satellite-derived precipitation products for streamflow simulation of a mountainous himalayan watershed: a study of Myagdi Khola in Kali Gandaki Basin, Nepal. Remote Sens. 15, 4762. https://doi.org/10.3390/rs15194762.

Ashouri, H., Hsu, K.-L., Sorooshian, S., Braithwaite, D.K., Knapp, K.R., Cecil, L.D., Nelson, B.R., Prat, O.P., 2015. PERSIANN-CDR: daily precipitation climate data record from multisatellite observations for hydrological and climate studies. Bull. Am. Meteorol. Soc. 96, 69–83. https://doi.org/10.1175/BAMS-D-13-00068.1.

Azimi, S., Massari, C., Formetta, G., Barbetta, S., Tazioli, A., Fronzi, D., Modanesi, S., Tarpanelli, A., Rigon, R., 2023. On understanding mountainous carbonate basins of the Mediterranean using parsimonious modeling solutions. Hydrol. Earth Syst. Sci. 27, 4485–4503. https://doi.org/10.5194/hess-27-4485-2023.

Baffaut, C., Benson, V.W., 2009. Modeling flow and pollutant transport in a karst watershed with SWAT. Trans. ASABE 52 (2), 469–479. https://doi.org/10.13031/2013.26840.

Bailly-Comte, V., Jourde, H., Roesch, A., Pistre, S., Batiot-Guilhe, C., 2008. Time series analyses for Karst/River interactions assessment: case of the Coulazou river (southern France). J. Hydrol. 349, 98–114. https://doi.org/10.1016/j.jhydrol.2007.10.028.

Bárdossy, A., Kilsby, C., Birkinshaw, S., Wang, N., Anwar, F., 2022. Is precipitation responsible for the most hydrological model uncertainty? Front. Water 4, 836554. https://doi.org/10.3389/frwa.2022.836554.

Bieger, K., Arnold, J.G., Rathjens, H., White, M.J., Bosch, D.D., Allen, P.M., Volk, M., Srinivasan, R., 2017. Introduction to SWAT+, a completely restructured version of the soil and water assessment tool. JAWRA J. Am. Water Resour. Assoc. 53, 115–130. https://doi.org/10.1111/1752-1688.12482.

Bitew, M.M., Gebremichael, M., Ghebremichael, L.T., Bayissa, Y.A., 2012. Evaluation of high-resolution satellite rainfall products through streamflow simulation in a hydrological modeling of a small mountainous watershed in Ethiopia. J. Hydrometeorol. 13, 338–350. https://doi.org/10.1175/2011JHM1292.1.

Bittner, D., Narany, T.S., Kohl, B., Disse, M., Chiogna, G., 2018. Modeling the hydrological impact of land use change in a dolomite-dominated karst system. J. Hydrol. 567, 267–279. https://doi.org/10.1016/j.jhydrol.2018.10.017.

Brocca, L., Ciabatta, L., Massari, C., Moramarco, T., Hahn, S., Hasenauer, S., Kidd, R., Dorigo, W., Wagner, W., Levizzani, V., 2014. Soil as a natural rain gauge: estimating global rainfall from satellite soil moisture data. J. Geophys. Res. Atmospheres 119, 5128–5141. https://doi.org/10.1002/2014JD021489.

Brocca, L., Filippucci, P., Hahn, S., Ciabatta, L., Massari, C., Camici, S., Schüller, L., Bojkov, B., Wagner, W., 2019. SM2RAIN–ASCAT (2007–2018): global daily satellite rainfall data from ASCAT soil moisture observations. Earth Syst. Sci. Data 11, 1583–1601. https://doi.org/10.5194/essd-11-1583-2019.

Butscher, C., Huggenberger, P., 2008. Intrinsic vulnerability assessment in karst areas: a numerical modeling approach. Water Resour. Res. 44. https://doi.org/10.1029/2007WR006277, 2007WR006277.

Camici, S., Ciabatta, L., Massari, C., Brocca, L., 2018. How reliable are satellite precipitation estimates for driving hydrological models: a verification study over the Mediterranean area. J. Hydrol. 563, 950–961. https://doi.org/10.1016/j.jhydrol.2018.06.067.

Chang, Y., Qi, Y., Wang, Z., 2024. Comprehensive evaluation of IMERG, ERA5-Land and their fusion products in the hydrological simulation of three karst catchments in Southwest China. J. Hydrol. Reg. Stud. 52, 101671. https://doi.org/10.1016/j.ejrh.2024.101671.

Chen, Z., Auler, A.S., Bakalowicz, M., Drew, D., Griger, F., Hartmann, J., Jiang, G., Moosdorf, N., Richts, A., Stevanovic, Z., Veni, G., Goldscheider, N., 2017. The World Karst Aquifer Mapping project: concept, mapping procedure and map of Europe. Hydrogeol. J. 25, 771–785. https://doi.org/10.1007/s10040-016-1519-3.

Chen, Y., Oliver, D.S., 2013. Levenberg–Marquardt forms of the iterative ensemble smoother for efficient history matching and uncertainty quantification. Comput. Geosci. 17, 689–703. https://doi.org/10.1007/s10596-013-9351-5.

Chen, M., Shi, W., Xie, P., Silva, V.B.S., Kousky, V.E., Wayne Higgins, R., Janowiak, J.E., 2008. Assessing objective techniques for gauge-based analyses of global daily precipitation. J. Geophys. Res. Atmospheres 113. https://doi.org/10.1029/2007JD009132, 2007JD009132.

Chiphang, N., Bandyopadhyay, A., Bhadra, A., 2020. Assessing the effects of snowmelt dynamics on streamflow and water balance components in an Eastern Himalayan River Basin Using SWAT Model. Environ. Model Assess. 25, 861–883. https://doi.org/10.1007/s10666-020-09716-8.

Cornes, R.C., Van Der Schrier, G., Van Den Besselaar, E.J.M., Jones, P.D., 2018. An ensemble version of the E-OBS temperature and precipitation data sets. J. Geophys. Res. Atmospheres 123, 9391–9409. https://doi.org/10.1029/2017JD028200.

Cousquer, Y., Jourde, H., 2022. Reducing uncertainty of karst aquifer modeling with complementary hydrological observations for the sustainable management of groundwater resources. J. Hydrol. 612, 128130. https://doi.org/10.1016/j.jhydrol.2022.128130.

Dal Soglio, L., Danquigny, C., Mazzilli, N., Emblanch, C., Massonnat, G., 2020. Modeling the matrix-conduit exchanges in both the epikarst and the transmission zone of karst systems. Water 12, 3219. https://doi.org/10.3390/w12113219.

Debroas, E.-J., 2009. Géologie du bassin versant du Baget (zone nord-pyrénéenne, Ariège, France): nouvelles observations et conséquences. STRATA 2, 46.

Déqué, M., Dreveton, C., Braun, A., Cariolle, D., 1994. The ARPEGE/IFS atmosphere model: a contribution to the French community climate modelling. Clim. Dyn. 10, 249–266. https://doi.org/10.1007/BF00208992.

Doherty, J., 2018. PEST Model-Independent Parameter Estimation User Manual, 7th ed. Watermark Numerical Computing, Brisbane, Queensland, Australia.

Dos Reis, J., Rennó, C., Lopes, E., 2017. Validation of satellite rainfall products over a mountainous watershed in a humid subtropical climate Region of Brazil. Remote Sens. 9, 1240. https://doi.org/10.3390/rs9121240.

Emmanuel, I., Payrastre, O., Andrieu, H., Zuber, F., 2017. A method for assessing the influence of rainfall spatial variability on hydrograph modeling. First case study in the Cevennes Region, southern France. J. Hydrol. 555, 314–322. https://doi.org/10.1016/j.jhydrol.2017.10.011.

Evensen, G., 1994. Sequential data assimilation with a nonlinear quasi-geostrophic model using Monte Carlo methods to forecast error statistics. J. Geophys. Res. Oceans 99, 10143–10162. https://doi.org/10.1029/94JC00572.

Fidelibus, M.D., Balacco, G., Gioia, A., Iacobellis, V., Spilotro, G., 2017. Mass transport triggered by heavy rainfall: the role of endorheic basins and epikarst in a regional karst aquifer: Epikarst under heavy rainfall causes temporary groundwater pollution. Hydrol. Process. 31, 394–408. https://doi.org/10.1002/hyp.11037.

Filippucci, P., Ciabatta, L., Mosaffa, H., Brocca, L., 2024. Improving the resolution of satellite precipitation products in Europe. Presented at the EGU General Assembly 2024, Vienna, Austria. doi: 10.5194/egusphere-egu24-16956.

Fiorillo, F., Guadagno, F.M., 2012. Long karst spring discharge time series and droughts occurrence in Southern Italy. Environ. Earth Sci. 65, 2273–2283. https://doi.org/10.1007/s12665-011-1495-9.

Fischer, P., Jardani, A., Lecoq, N., 2018. Hydraulic tomography of discrete networks of conduits and fractures in a karstic aquifer by using a deterministic inversion algorithm. Adv. Water Resour. 112, 83–94. https://doi.org/10.1016/j.advwatres.2017.11.029.

Fleury, P., Plagnes, V., Bakalowicz, M., 2007. Modelling of the functioning of karst aquifers with a reservoir model: application to Fontaine de Vaucluse (South of France). J. Hydrol. 345, 38–49. https://doi.org/10.1016/j.jhydrol.2007.07.014.

Fleury, P., Ladouche, B., Conroux, Y., Jourde, H., Dörfliger, N., 2009. Modelling the hydrologic functions of a karst aquifer under active water management – The Lez spring. J. Hydrol. 365, 235–243. https://doi.org/10.1016/j.jhydrol.2008.11.037.

Fumière, Q., Déqué, M., Nuissier, O., Somot, S., Alias, A., Caillaud, C., Laurantin, O., Seity, Y., 2020. Extreme rainfall in Mediterranean France during the fall: added value of the CNRM-AROME convection-permitting regional climate model. Clim. Dyn. 55, 77–91. https://doi.org/10.1007/s00382-019-04898-8.

Funk, C., Peterson, P., Landsfeld, M., Pedreros, D., Verdin, J., Shukla, S., Husak, G., Rowland, J., Harrison, L., Hoell, A., Michaelsen, J., 2015. The climate hazards infrared precipitation with stations—a new environmental record for monitoring extremes. Sci. Data 2, 150066. https://doi.org/10.1038/sdata.2015.66.

Furl, C., Ghebreyesus, D., Sharif, H., 2018. Assessment of the performance of satellite-based precipitation products for flood events across diverse spatial scales using

GSSHA modeling system. Geosciences 8, 191. https://doi.org/10.3390/geosciences8060191.
Gaillardet, J., Braud, I., Hankard, F., Anquetin, S., Bour, O., Dorfliger, N., de Dreuzy, J.R., Galle, S., Galy, C., Gogo, S., Gourcy, L., Habets, F., Laggoun, F., Longuevergne, L., Le Borgne, T., Naaim-Bouvet, F., Nord, G., Simonneaux, V., Six, D., Tallec, T., Valentin, C., Abril, G., Allemand, P., Arènes, A., Arfib, B., Arnaud, L., Arnaud, N., Arnaud, P., Audry, S., Comte, V.B., Batiot, C., Battais, A., Bellot, H., Bernard, E., Bertrand, C., Bessière, H., Binet, S., Bodin, J., Bodin, X., Boithias, L., Bouchez, J., Boudevillain, B., Moussa, I.B., Branger, F., Braun, J.J., Brunet, P., Caceres, B., Calmels, D., Cappelaere, B., Celle-Jeanton, H., Chabaux, F., Chalikakis, K., Champollion, C., Copard, Y., Cotel, C., Davy, P., Deline, P., Delrieu, G., Demarty, J., Dessert, C., Dumont, M., Emblanch, C., Ezzahar, J., Estèves, M., Favier, V., Faucheux, M., Filizola, N., Flammarion, P., Floury, P., Fovet, O., Fournier, M., Francez, A.J., Gandois, L., Gascuel, C., Gayer, E., Genthon, C., Gérard, M.F., Gilbert, D., Gouttevin, I., Grippa, M., Gruau, G., Jardani, A., Jeanneau, L., Join, J.L., Jourde, H., Karbou, F., Labat, D., Lagadeuc, Y., Lajeunesse, E., Lastennet, R., Lavado, W., Lawin, E., Lebel, T., Le Bouteiller, C., Legout, C., Lejeune, Y., Le Meur, E., Le Moigne, N., Lions, J., Lucas, A., Malet, J.P., Marais-Sicre, C., Maréchal, J.C., Marlin, C., Martin, P., Martins, J., Martinez, J.M., Massei, N., Mauclerc, A., Mazzilli, N., Molénat, J., Moreira-Turcq, P., Mougin, E., Morin, S., Ngoupayou, J.N., Panthou, G., Peugeot, C., Picard, G., Pierret, M.C., Porel, G., Probst, A., Probst, J.L., Rabatel, A., Raclot, D., Ravanel, L., Rejiba, F., René, P., Ribolzi, O., Riotte, J., Rivière, A., Robain, H., Ruiz, L., Sanchez-Perez, J.M., Santini, W., Sauvage, S., Schoeneich, P., Seidel, J.L., Sekhar, M., Sengtaheuanghoung, O., Silvera, N., Steinmann, M., Soruco, A., Tallec, G., Thibert, E., Lao, D.V., Vincent, C., Viville, D., Wagnon, P., Zitouna, R., 2018. OZCAR: The French network of critical zone observatories. Vadose Zone J. 17, 1–24. https://doi.org/10.2136/vzj2018.04.0067.
Galván, L., Olías, M., Izquierdo, T., Cerón, J.C., Fernández de Villarán, R., 2014. Rainfall estimation in SWAT: an alternative method to simulate orographic precipitation. J. Hydrol. 509, 257–265. https://doi.org/10.1016/j.jhydrol.2013.11.044.
Gan, F., Gao, Y., Xiao, L., Qin, L., Huang, Y., Zhang, H., 2020. An applicability evaluation of version 05 IMERG precipitation products over a coastal basin located in the tropics with hilly and karst combined Landform. China. Int. J. Remote Sens. 41, 4570–4589. https://doi.org/10.1080/01431161.2020.1723174.
Gan, F., Gao, Y., Xiao, L., 2021. Comprehensive validation of the latest IMERG V06 precipitation estimates over a basin coupled with coastal locations, tropical climate and hill-karst combined landform. Atmospheric Res. 249, 105293. https://doi.org/10.1016/j.atmosres.2020.105293.
Geng, X., Zhang, C., Zhang, F., Chen, Z., Nie, Z., Liu, M., 2021. Hydrological modeling of karst watershed containing subterranean river using a modified SWAT model: a case study of the Daotian River Basin, Southwest China. Water 13 (24), 3552. https://doi.org/10.3390/w13243552.
Geyer, T., Birk, S., Reimann, T., Dörfliger, N., Sauter, M., 2013. Differentiated characterization of karst aquifers: some contributions. Carbonates Evaporites 28, 41–46. https://doi.org/10.1007/s13146-013-0150-9.
Ghasemizadeh, R., Hellweger, F., Butscher, C., Padilla, I., Vesper, D., Field, M., Alshawabkeh, A., 2012. Review: Groundwater flow and transport modeling of karst aquifers, with particular reference to the North Coast Limestone aquifer system of Puerto Rico. Hydrogeol. J. 20, 1441–1461. https://doi.org/10.1007/s10040-012-0897-4.
Gill, L.W., Schuler, P., Duran, L., Morrissey, P., Johnston, P.M., 2021. An evaluation of semidistributed-pipe-network and distributed-finite-difference models to simulate karst systems. Hydrogeol. J. 29, 259–279. https://doi.org/10.1007/s10040-020-02241-8.
Goldscheider, N., Chen, Z., Auler, A.S., Bakalowicz, M., Broda, S., Drew, D., Hartmann, J., Jiang, G., Moosdorf, N., Stevanovic, Z., Veni, G., 2020. Global distribution of carbonate rocks and karst water resources. Hydrogeol. J. 28, 1661–1677. https://doi.org/10.1007/s10040-020-02139-5.
Grusson, Y., Sun, X., Gascoin, S., Sauvage, S., Raghavan, S., Anctil, F., et al., 2015. Assessing the capability of the SWAT model to simulate snow, snow melt and streamflow dynamics over an alpine watershed. J. Hydrol. 531 (Part 3), 574. https://doi.org/10.1016/j.jhydrol.2015.10.070.
Gupta, H.V., Sorooshian, S., Yapo, P.O., 1999. Status of automatic calibration for hydrologic models: comparison with multilevel expert calibration. J. Hydrol. Eng. 4, 135–143. https://doi.org/10.1061/(ASCE)1084-0699(1999)4:2(135).
Gupta, H.V., Kling, H., Yilmaz, K.K., Martinez, G.F., 2009. Decomposition of the mean squared error and NSE performance criteria: implications for improving hydrological modelling. J. Hydrol. 377, 80–91. https://doi.org/10.1016/j.jhydrol.2009.08.003.
Hartmann, A., Lange, J., Vivó Aguado, À., Mizyed, N., Smiatek, G., Kunstmann, H., 2012. A multi-model approach for improved simulations of future water availability at a large Eastern Mediterranean karst spring. J. Hydrol. 468–469, 130–138. https://doi.org/10.1016/j.jhydrol.2012.08.024.
Hartmann, A., Barberá, J.A., Lange, J., Andreo, B., Weiler, M., 2013. Progress in the hydrologic simulation of time variant recharge areas of karst systems – Exemplified at a karst spring in Southern Spain. Adv. Water Resour. 54, 149–160. https://doi.org/10.1016/j.advwatres.2013.01.010.
Haylock, M.R., Hofstra, N., Klein Tank, A.M.G., Klok, E.J., Jones, P.D., New, M., 2008. A European daily high-resolution gridded data set of surface temperature and precipitation for 1950–2006. J. Geophys. Res. Atmospheres 113. https://doi.org/10.1029/2008JD010201, 2008JD010201.
Hersbach, H., Bell, B., Berrisford, P., Hirahara, S., Horányi, A., Muñoz-Sabater, J., Nicolas, J., Peubey, C., Radu, R., Schepers, D., Simmons, A., Soci, C., Abdalla, S., Abellan, X., Balsamo, G., Bechtold, P., Biavati, G., Bidlot, J., Bonavita, M., De Chiara, G., Dahlgren, P., Dee, D., Diamantakis, M., Dragani, R., Flemming, J., Forbes, R., Fuentes, M., Geer, A., Haimberger, L., Healy, S., Hogan, R.J., Hólm, E., Janisková, M., Keeley, S., Laloyaux, P., Lopez, P., Lupu, C., Radnoti, G., De Rosnay, P., Rozum, I., Vamborg, F., Villaume, S., Thépaut, J., 2020. The ERA5 global reanalysis. Q. J. r. Meteorol. Soc. 146, 1999–2049. https://doi.org/10.1002/qj.3803.
Huang, Y., Bárdossy, A., Zhang, K., 2019. Sensitivity of hydrological models to temporal and spatial resolutions of rainfall data. Hydrol. Earth Syst. Sci. 23, 2647–2663. https://doi.org/10.5194/hess-23-2647-2019.
Huffman, G.J., Bolvin, D.T., Braithwaite, D., Hsu, K., Joyce, R., Kidd, C., Nelkin, E.J., Sorooshian, S., Tan, J., Xie, P., 2019. NASA Global Precipitation Measurement (GPM) Integrated Multi-satellitE Retrievals for GPM (IMERG). Algorithm theoretical basis document (ATBD) version, 4(26), p.30. https://gpm.nasa.gov/sites/default/files/document_files/IMERG_ATBD_V06.pdf.
Jeannin, P.-Y., Artigue, G., Butscher, C., Chang, Y., Charlier, J.-B., Duran, L., Gill, L., Hartmann, A., Johannet, A., Jourde, H., Kavousi, A., Liesch, T., Liu, Y., Lüthi, M., Malard, A., Mazzilli, N., Pardo-Igúzquiza, E., Thiéry, D., Reimann, T., Schuler, P., Wöhling, T., Wunsch, A., 2021. Karst modelling challenge 1: Results of hydrological modelling. J. Hydrol. 600, 126508. https://doi.org/10.1016/j.jhydrol.2021.126508.
Jiang, S., Wei, L., Ren, L., Zhang, L., Wang, M., Cui, H., 2023. Evaluation of IMERG, TMPA, ERA5, and CPC precipitation products over mainland China: Spatiotemporal patterns and extremes. Water Sci. Eng. 16, 45–56. https://doi.org/10.1016/j.wse.2022.05.001.
Johannet, A., Mangin, A., Vayssade, B., 2008. Modélisation d'un système karstique par réseaux de neurones : simulation des débits du karst du Baget, France. Collect. EDYTEM Cah. Géographie 7, 51–62. doi: 10.3406/edyte.2008.1054.
Jourde, H., Massei, N., Mazzilli, N., Binet, S., Batiot-Guilhe, C., Labat, D., Steinmann, M., Bailly-Comte, V., Seidel, J.L., Arfib, B., Charlier, J.B., Guinot, V., Jardani, A., Fournier, M., Aliouache, M., Babic, M., Bertrand, C., Brunet, P., Boyer, J.F., Bricquet, J.P., Camboulive, T., Carrière, S.D., Celle-Jeanton, H., Chalikakis, K., Chen, N., Cholet, C., Clauzon, V., Soglio, L.D., Danquigny, C., Défargue, C., Denimal, S., Emblanch, C., Hernandez, F., Gillon, M., Gutierrez, A., Sanchez, L.H., Hery, M., Houillon, N., Johannet, A., Jouves, J., Jozja, N., Ladouche, B., Leonardi, V., Lorette, G., Loup, C., Marchand, P., de Montety, V., Muller, R., Ollivier, C., Sivelle, V., Lastennet, R., Lecoq, N., Maréchal, J.C., Perotin, L., Perrin, J., Petre, M.A., Peyraube, N., Pistre, S., Plagnes, V., Probst, A., Probst, J.L., Simler, R., Stefani, V., Valdes-Lao, D., Viseur, S., Wang, X., 2018. SNO KARST: a French network of observatories for the multidisciplinary study of critical zone processes in karst watersheds and aquifers. Vadose Zone J. 17, 1–18. https://doi.org/10.2136/vzj2018.04.0094.
Karger, D.N., Conrad, O., Böhner, J., Kawohl, T., Kreft, H., Soria-Auza, R.W., Zimmermann, N.E., Linder, H.P., Kessler, M., 2017. Climatologies at high resolution for the earth's land surface areas. Sci. Data 4, 170122. https://doi.org/10.1038/sdata.2017.122.
Khan, A., Koch, M., 2018. Correction and informed regionalization of precipitation data in a high mountainous region (Upper Indus Basin) and its effect on SWAT-modelled discharge. Water 10, 1557. https://doi.org/10.3390/w10111557.
Klaas, D.K.S.Y., Imteaz, M.A., Sudiayem, I., Klaas, E.M.E., Klaas, E.C.M., 2020. Assessing climate changes impacts on tropical karst catchment: Implications on groundwater resource sustainability and management strategies. J. Hydrol. 582, 124426. https://doi.org/10.1016/j.jhydrol.2019.124426.
Labat, D., Ababou, R., Mangin, A., 1999. Linear and nonlinear input/output models for karstic springflow and flood prediction at different time scales. Stoch. Environ. Res. Risk Assess. 13, 337. https://doi.org/10.1007/s004770050055.
Labat, D., Ababou, R., Mangin, A., 2000a. Rainfall–runoff relations for karstic springs. Part I: convolution and spectral analyses. J. Hydrol. 238, 123–148. https://doi.org/10.1016/S0022-1694(00)00321-8.
Labat, D., Ababou, R., Mangin, A., 2000b. Rainfall–runoff relations for karstic springs. Part II: continuous wavelet and discrete orthogonal multiresolution analyses. J. Hydrol. 238, 149–178. https://doi.org/10.1016/S0022-1694(00)00322-X.
Labat, D., Argouze, R., Mazzilli, N., Ollivier, C., Sivelle, V., 2022. Impact of withdrawals on karst watershed water supply. Water 14, 1339. https://doi.org/10.3390/w14091339.
Le Roy, B., Lemonsu, A., Kounkou-Arnaud, R., Brion, D., Masson, V., 2020. Long time series spatialized data for urban climatological studies: a case study of Paris, France. Int. J. Climatol. 40, 3567–3584. https://doi.org/10.1002/joc.6414.
Li, H., Ma, J., Yang, Y., Niu, L., Lu, X., 2023. Performance of frequency-corrected precipitation in ungauged high mountain hydrological simulation. Water 15 (8), 1461. https://doi.org/10.3390/w15081461.
Li, J., Yuan, D., Liu, J., Jiang, Y., Chen, Y., Hsu, K.L., Sorooshian, S., 2019. Predicting floods in a large karst river basin by coupling PERSIANN-CCS QPEs with a physically based distributed hydrological model. Hydrol. Earth Syst. Sci. 23, 1505–1532. https://doi.org/10.5194/hess-23-1505-2019.
Lobligeois, F., Andréassian, V., Perrin, C., Tabary, P., Loumagne, C., 2014. When does higher spatial resolution rainfall information improve streamflow simulation? An evaluation using 3620 flood events. Hydrol. Earth Syst. Sci. 18, 575–594. https://doi.org/10.5194/hess-18-575-2014.
Londhe, D.S., Katpatal, Y.B., Bokde, N.D., 2023. Performance assessment of bias correction methods for precipitation and temperature from CMIP5 model simulation. Appl. Sci. 13 (16), 9142. https://doi.org/10.3390/app13169142.
Maggioni, V., Massari, C., 2018. On the performance of satellite precipitation products in riverine flood modeling: a review. J. Hydrol. 558, 214–224. https://doi.org/10.1016/j.jhydrol.2018.01.039.
Mangin, A., 1975. Contribution à l'étude hydrodynamique des aquifères karstiques (Thesis). Université de Dijon, France.
Mazzilli, N., Guinot, V., Jourde, H., Lecoq, N., Labat, D., Arfib, B., Baudement, C., Danquigny, C., Dal Soglio, L., Bertin, D., 2019. KarstMod: a modelling platform for

rainfall – discharge analysis and modelling dedicated to karst systems. Environ. Model. Softw. 122, 103927. https://doi.org/10.1016/j.envsoft.2017.03.015.
Mo, C., Zhang, M., Ruan, Y., Qin, J., Wang, Y., Sun, G., Xing, Z., 2020. Accuracy analysis of IMERG Satellite rainfall data and its application in long-term runoff simulation. Water 12, 2177. https://doi.org/10.3390/w12082177.
Mo, C., Chen, X., Lei, X., Wang, Y., Ruan, Y., Lai, S., Xing, Z., 2022. Evaluation of hydrological simulation in a Karst Basin with different calibration methods and rainfall inputs. Atmosphere 13, 844. https://doi.org/10.3390/atmos13050844.
Mo, C., Lai, S., Yang, Q., Huang, K., Lei, X., Yang, L., Yan, Z., Jiang, C., 2023. A comprehensive assessment of runoff dynamics in response to climate change and human activities in a typical karst watershed, southwest China. J. Environ. Manage. 332, 117380. https://doi.org/10.1016/j.jenvman.2023.117380.
Monteith, J.L., 1965. Evaporation and environment. Symp. Soc. Exp. Biol. 19, 205–234.
Moriasi, D.N., Gitau, M.W., Pai, N., Daggupati, P., 2015. Hydrologic and water quality models: performance measures and evaluation criteria. Trans. ASABE 58, 1763–1785. https://doi.org/10.13031/trans.58.10715.
Morris, M.D., 1991. Factorial sampling plans for preliminary computational experiments. Technometrics 33, 161–174. https://doi.org/10.1080/00401706.1991.10484804.
Moucha, A., Hanich, L., Tramblay, Y., Saaidi, A., Gascoin, S., Martin, E., Le Page, M., Bouras, E., Szczypta, C., Jarlan, L., 2021. Present and future high-resolution climate forcings over semiarid catchments: case of the tensift (Morocco). Atmosphere 12, 370. https://doi.org/10.3390/atmos12030370.
Muñoz-Sabater, J., Dutra, E., Agustí-Panareda, A., Albergel, C., Arduini, G., Balsamo, G., Boussetta, S., Choulga, M., Harrigan, S., Hersbach, H., Martens, B., Miralles, D.G., Piles, M., Rodríguez-Fernández, N.J., Zsoter, E., Buontempo, C., Thépaut, J.-N., 2021. ERA5-Land: a state-of-the-art global reanalysis dataset for land applications. Earth Syst. Sci. Data 13, 4349–4383. https://doi.org/10.5194/essd-13-4349-2021.
Nash, J.E., Sutcliffe, J.V., 1970. River flow forecasting through conceptual models part I — a discussion of principles. J. Hydrol. 10, 282–290. https://doi.org/10.1016/0022-1694(70)90255-6.
Neitsch, S.L., Arnold, J.G., Kiniry, J.R., Williams, J.R., 2011. Soil and Water Assessment Tool Theoretical Documentation. Texas Water Resources Institute, College Station, TX, USA.
Nerantzaki, S.D., Hristopulos, D.T., Nikolaidis, N.P., 2020. Estimation of the uncertainty of hydrologic predictions in a karstic Mediterranean watershed. Sci. Total Environ. 717, 137131. https://doi.org/10.1016/j.scitotenv.2020.137131.
Nerantzaki, S.D., Nikolaidis, N.P., 2020. The response of three Mediterranean karst springs to drought and the impact of climate change. J. Hydrol. 591, 125296. https://doi.org/10.1016/j.jhydrol.2020.125296.
Nguyen, V.T., Dietrich, J., Uniyal, B., 2020. Modeling interbasin groundwater flow in karst areas: Model development, application, and calibration strategy. Environ. Model. Softw. 124, 104606. https://doi.org/10.1016/j.envsoft.2019.104606.
Nguyen, P., Ombadi, M., Sorooshian, S., Hsu, K., AghaKouchak, A., Braithwaite, D., Ashouri, H., Thorstensen, A.R., 2018. The PERSIANN family of global satellite precipitation data: a review and evaluation of products. Hydrol. Earth Syst. Sci. 22, 5801–5816. https://doi.org/10.5194/hess-22-5801-2018.
Nikolaidis, N.P., Bouraoui, F., Bidoglio, G., 2013. Hydrologic and geochemical modeling of a karstic Mediterranean watershed. J. Hydrol. 477, 129–138. https://doi.org/10.1016/j.jhydrol.2012.11.018.
Ollivier, C., Chalikakis, K., Mazzilli, N., Kazakis, N., Lecomte, Y., Danquigny, C., Emblanch, C., 2019. Challenges and limitations of karst aquifer vulnerability mapping based on the PaPRIKa method—application to a large european karst aquifer (Fontaine de Vaucluse, France). Environments 6, 39. https://doi.org/10.3390/environments6030039.
Ollivier, C., Mazzilli, N., Olioso, A., Chalikakis, K., Carrière, S.D., Danquigny, C., Emblanch, C., 2020. Karst recharge-discharge semi distributed model to assess spatial variability of flows. Sci. Total Environ. 703, 134368. https://doi.org/10.1016/j.scitotenv.2019.134368.
Padilla, A., Pulido-Bosch, A., Mangin, A., 1994. Relative importance of basefow and quickfow from hydrographs of karst spring. Groundwater 32, 267–277. https://doi.org/10.1111/j.1745-6584.1994.tb00641.x.
Paiva, I., Cunha, L., 2020. Characterization of the hydrodynamic functioning of the Degracias-Sicó Karst Aquifer. Portugal. Hydrogeol. J. 28, 2613–2629. https://doi.org/10.1007/s10040-020-02201-2.
Palanisamy, B., Workman, S.R., 2015. Hydrologic modeling of flow through sinkholes located in streambeds of cane run stream. Kentucky. J. Hydrol. Eng. 20 (5), 04014066. https://doi.org/10.1061/(ASCE)HE.1943-5584.0001060.
Peinó, E., Bech, J., Udina, M., Polls, F., 2024. Disentangling satellite precipitation estimate errors of heavy rainfall at the daily and sub-daily scales in the Western Mediterranean. Remote Sens. 16, 457. https://doi.org/10.3390/rs16030457.
Pool, S., Vis, M., Seibert, J., 2018. Evaluating model performance: towards a non-parametric variant of the Kling-Gupta efficiency. Hydrol. Sci. J. 63, 1941–1953. https://doi.org/10.1080/02626667.2018.1552002.
Quintana-Seguí, P., Le Moigne, P., Durand, Y., Martin, E., Habets, F., Baillon, M., Canellas, C., Franchisteguy, L., Morel, S., 2008. Analysis of near-surface atmospheric variables: validation of the SAFRAN analysis over France. J. Appl. Meteorol. Climatol. 47, 92–107. https://doi.org/10.1175/2007JAMC1636.1.
Richieri, B., Bittner, D., Sivelle, V., Hartmann, A., Labat, D., Chiogna, G., 2024. On the value of hydrochemical data for the interpretation of flow and transport processes in the Baget karst system, France. Hydrogeol. J. 32, 1537–1555. https://doi.org/10.1007/s10040-024-02801-2.
Ritter, B., Geleyn, J.-F., 1992. A comprehensive radiation scheme for numerical weather prediction models with potential applications in climate simulations. Mon. Weather Rev. 120, 303–325. https://doi.org/10.1175/1520-0493(1992)120<0303:ACRSFN>2.0.CO;2.
Ruiz, M.C., Valdés-Abellán, J., Pla, C., Fernández-Mejuto, M., Benavente, D., 2022. Land cover changes and their influence on recharge in a mediterranean karstic aquifer (Alicante, Spain). Land 12, 128. https://doi.org/10.3390/land12010128.
Salmani-Dehaghi, N., Samani, N., 2021. Development of bias-correction PERSIANN-CDR models for the simulation and completion of precipitation time series. Atmos. Environ. 246, 117981. https://doi.org/10.1016/j.atmosenv.2020.117981.
Satgé, F., Ruelland, D., Bonnet, M.-P., Molina, J., Pillco, R., 2019. Consistency of satellite-based precipitation products in space and over time compared with gauge observations and snow- hydrological modelling in the Lake Titicaca region. Hydrol. Earth Syst. Sci. 23, 595–619. https://doi.org/10.5194/hess-23-595-2019.
Shirafkan, M., Mohammadi, Z., Kavousi, A., Sivelle, V., Labat, D., Reimann, T., 2023. Toward the estimation of the transfer coefficient in karst systems: Using baseflow recession coefficient under matrix-restrained flow regime. J. Hydrol. 620, 129441. https://doi.org/10.1016/j.jhydrol.2023.129441.
Sivelle, V., Jourde, H., Bittner, D., Mazzilli, N., Tramblay, Y., 2021. Assessment of the relative impacts of climate changes and anthropogenic forcing on spring discharge of a Mediterranean karst system. J. Hydrol. 598, 126396. https://doi.org/10.1016/j.jhydrol.2021.126396.
Sivelle, V., Jourde, H., Bittner, D., Richieri, B., Labat, D., Hartmann, A., Chiogna, G., 2022. Considering land cover and land use (LCLU) in lumped parameter modeling in forest dominated karst catchments. J. Hydrol. 612, 128264. https://doi.org/10.1016/j.jhydrol.2022.128264.
Sivelle, V., Cinkus, G., Mazzilli, N., Labat, D., Arfib, B., Massei, N., Cousquer, Y., Bertin, D., Jourde, H., 2023. Improvement of the KarstMod modeling platform for a better assessment of karst groundwater resources (preprint). Groundwater Hydrol/Modelling Approaches. https://doi.org/10.5194/hess-2023-17.
Sivelle, V., Labat, D., 2019. Short-term variations in tracer-test responses in a highly karstified watershed. Hydrogeol. J. 27, 2061–2075. https://doi.org/10.1007/s10040-019-01968-3.
Sivelle, V., Labat, D., Mazzilli, N., Massei, N., Jourde, H., 2019. Dynamics of the flow exchanges between matrix and conduits in karstified watersheds at multiple temporal scales. Water 11, 569. https://doi.org/10.3390/w11030569.
Sloan, P.G., Moore, I.D., 1984. Modeling subsurface stormflow on steeply sloping forested watersheds. Water Resour. Res. 20, 1815–1822. https://doi.org/10.1029/WR020i012p01815.
Stevanović, Z., 2019. Karst waters in potable water supply: a global scale overview. Environ. Earth Sci. 78, 662. https://doi.org/10.1007/s12665-019-8670-9.
Tabary, P., 2007. The new french operational radar rainfall product. Part i: Methodology. Weather Forecast. 22, 393–408. https://doi.org/10.1175/WAF1004.1.
Tabary, P., Dupuy, P., L'Henaff, G., Gueguen, C., Moulin, L., Laurantin, O., Merlier, C., Soubeyroux, J.-M., 2012. A 10-year (1997–2006) reanalysis of Quantitative Precipitation Estimation over France: methodology and first results. In: Presented at the Weather radar and hydrology. IAHS-AISH Publication, pp. 255–260.
Taheri, K., Taheri, M., Parise, M., 2016. Impact of intensive groundwater exploitation on an unprotected covered karst aquifer: a case study in Kermanshah Province, western Iran. Environ. Earth Sci. 75, 1221. https://doi.org/10.1007/s12665-016-5995-5.
Tritz, S., Guinot, V., Jourde, H., 2011. Modelling the behaviour of a karst system catchment using non-linear hysteretic conceptual model. J. Hydrol. 397, 250–262. https://doi.org/10.1016/j.jhydrol.2010.12.001.
Tuo, Y., Duan, Z., Disse, M., Chiogna, G., 2016. Evaluation of precipitation input for SWAT modeling in Alpine catchment: a case study in the Adige river basin (Italy). Sci. Total Environ. 573, 66–82. https://doi.org/10.1016/j.scitotenv.2016.08.034.
Uhlenbrook, S., Roser, S., Tilch, N., 2004. Hydrological process representation at the meso-scale: the potential of a distributed, conceptual catchment model. J. Hydrol. 291, 278–296. https://doi.org/10.1016/j.jhydrol.2003.12.038.
Ulloa-Cedamanos, F., Probst, J.-L., Binet, S., Camboulive, T., Payre-Suc, V., Pautot, C., Bakalowicz, M., Beranger, S., Probst, A., 2020. A forty-year karstic critical zone survey (Baget Catchment, Pyrenees-France): lithologic and hydroclimatic controls on seasonal and inter-annual variations of stream water chemical composition, pCO2, and carbonate equilibrium. Water 12 (5), 1227. https://doi.org/10.3390/w12051227.
USDA-SCS, 1972. National Engineering Handbook, Section 4: Hydrology. USDA, Washington, D.C.
Van Leeuwen, P.J., Evensen, G., 1996. Data assimilation and inverse methods in terms of a probabilistic formulation. Mon. Weather Rev. 124, 2898–2913. https://doi.org/10.1175/1520-0493(1996)124<2898:DAAIMI>2.0.CO;2.
Vidal, J.-P., Martin, E., Franchistéguy, L., Baillon, M., Soubeyroux, J.-M., 2010. A 50-year high-resolution atmospheric reanalysis over France with the Safran system: a 50-year high-resolution atmospheric reanalysis over France. Int. J. Climatol. 30, 1627–1644. https://doi.org/10.1002/joc.2003.
Wagner, W., Hahn, S., Kidd, R., Melzer, T., Bartalis, Z., Hasenauer, S., Figa-Saldaña, J., De Rosnay, P., Jann, A., Schneider, S., Komma, J., Kubu, G., Brugger, K., Aubrecht, C., Züger, J., Gangkofner, U., Kienberger, S., Brocca, L., Wang, Y., Blöschl, G., Eitzinger, J., Steinnocher, K., 2013. The ASCAT soil moisture product: a review of its specifications, validation results, and emerging applications. Meteorol. z. 22, 5–33. https://doi.org/10.1127/0941-2948/2013/0399.
Wang, Y., Brubaker, K., 2014. Implementing a nonlinear groundwater module in the soil and water assessment tool (SWAT): nonlinear groundwater module in swat. Hydrol. Process. 28 (9), 3388–3403. https://doi.org/10.1002/hyp.9893.
Wang, Y., Shao, J., Su, C., Cui, Y., Zhang, Q., 2019. The application of improved SWAT model to hydrological cycle study in karst area of South China. Sustainability 11 (18), 5024. https://doi.org/10.3390/su11185024.
Wang, Z., Zhong, R., Lai, C., 2017. Evaluation and hydrologic validation of TMPA satellite precipitation product downstream of the Pearl River Basin, China. Hydrol. Process. 31, 4169–4182. https://doi.org/10.1002/hyp.11350.

Welter, D.E., White, J.T., Hunt, R.J., Doherty, J.E., 2015. Approaches in highly parameterized inversion—PEST++ Version 3, a Parameter ESTimation and uncertainty analysis software suite optimized for large environmental models: U.S. Geological Survey Techniques and Methods (Techniques and Methods No. book 7, chap. C12). U.S. Geological Survey Techniques and Methods.

White, J.T., 2018. A model-independent iterative ensemble smoother for efficient history-matching and uncertainty quantification in very high dimensions. Environ. Model. Softw. 109, 191–201. https://doi.org/10.1016/j.envsoft.2018.06.009.

White, J.T., Hunt, R.J., Fienen, M.N., Doherty, J.E., 2020. Approaches to Highly Parameterized Inversion: PEST++ Version 5, a Software Suite for Parameter Estimation, Uncertainty Analysis, Management Optimization and Sensitivity Analysis, U.S. Geological Survey Techniques and Methods 7C26.

Wu, X., Su, J., Ren, W., Lü, H., Yuan, F., 2023. Statistical comparison and hydrological utility evaluation of ERA5-Land and IMERG precipitation products on the Tibetan Plateau. J. Hydrol. 620, 129384. https://doi.org/10.1016/j.jhydrol.2023.129384.

Wu, J., Zheng, H., Xi, Y., 2019. SWAT-based runoff simulation and runoff responses to climate change in the headwaters of the Yellow River, China. Atmosphere 10 (9), 509. https://doi.org/10.3390/atmos10090509.

Xie, P., Chen, M., Yang, S., Yatagai, A., Hayasaka, T., Fukushima, Y., Liu, C., 2007. A Gauge-based analysis of daily precipitation over East Asia. J. Hydrometeorol. 8, 607–626. https://doi.org/10.1175/JHM583.1.

Yactayo, G., 2009. Modification of the SWAT Model to Simulate Hydrologic Processes in a Karst-influenced Watershed. Virginia Polytechnic Institute and State University, Blacksburg, Virginia. Masters Thesis.

Ye, J., Lu, Y., Yang, X., He, Z., Huang, P., Zheng, X., 2023. Bias correction of hourly satellite precipitation products and their application in hydrological modeling in a Hilly Watershed, China. Water 16, 49. https://doi.org/10.3390/w16010049.

Zhang, Y., Su, F., Hao, Z., Xu, C., Yu, Z., Wang, L., Tong, K., 2015. Impact of projected climate change on the hydrology in the headwaters of the Yellow River basin. Hydrol. Process. 29 (20), 4379–4397. https://doi.org/10.1002/hyp.8171.

Zhang, Y., Hanati, G., Danierhan, S., Liu, Q., Xu, Z., 2020. Evaluation and comparison of daily GPM/TRMM precipitation products over the tianshan mountains in China. Water 12, 3088. https://doi.org/10.3390/w12113088.

Zhao, L., Yang, Y., Cao, J., Wang, Z., Luan, S., Xia, R., 2021. Applying a modified conduit flow process to understand conduit-matrix exchange of a karst aquifer. China Geol. 4, 1–8. https://doi.org/10.31035/cg2021046.

Zhou, Y., Zhao, L., Cao, J., Wang, Y., 2022. Using an improved SWAT model to simulate karst sinkholes: a case Study in Southwest China. Front. Environ. Sci. 10, 950098. https://doi.org/10.3389/fenvs.2022.950098.